

# Middle atmosphere response to the solar cycle in irradiance and ionizing particle precipitation

K. Semeniuk<sup>1</sup>, V. I. Fomichev<sup>1</sup>, J. C. McConnell<sup>1</sup>, C. Fu<sup>2</sup>, S. M. L. Melo<sup>2</sup>, and I. G. Usoskin<sup>3</sup>

<sup>1</sup>Department of Earth and Space Science and Engineering, York University, Toronto, Ontario, Canada

<sup>2</sup>Canadian Space Agency, St.-Hubert, Quebec, Canada

<sup>3</sup>Sodankylä Geophysical Laboratory, University of Oulu, Oulu, Finland

*Correspondence to:* K. Semeniuk (kirill@nimbus.yorku.ca)

**Abstract.** The impact of NO<sub>x</sub> and HO<sub>x</sub> production by three types of energetic particle precipitation (EPP), aurora, solar proton events and galactic cosmic rays is examined using a chemistry climate model. This process study uses ensemble simulations forced by transient EPP derived from observations with one-year repeating sea surface temperatures and fixed chemical boundary conditions were conducted for cases with and without solar cycle in irradiance. Our model results show a wintertime polar stratosphere ozone reduction of between 3 and 10% in agreement with previous studies. EPP is found to modulate the radiative solar cycle effect in the middle atmosphere in a significant way, bringing temperature and ozone variations closer to observed patterns. The Southern Hemisphere polar vortex undergoes an intensification from solar minimum to solar maximum instead of a weakening. This changes the solar cycle variation of the Brewer-Dobson circulation, with a weakening during solar maxima compared to solar minima. In response, the tropical tropopause temperature manifests a statistically significant solar cycle variation resulting in about 4% more water vapour transported into the lower tropical stratosphere during solar maxima compared to solar minima. This has implications for surface temperature variation due to the associated change in radiative forcing.

## 15 1 Introduction

Although the field of research on the influence of the variability of solar radiation and particle flux on the atmosphere is fast growing, great uncertainty remains concerning impacts and the mechanisms involved. Traditionally, modeling studies of solar variability effects on the climate system have focused on two basic ideas: (1) direct forcing of the troposphere by surface warming asso-

20 ciated with changes in the total solar irradiance (TSI) or, in a more complex scenario, modulation  
of the atmosphere-ocean interactions producing internal oscillations (see for example White et al.,  
1997; White, 2006); and (2) forcing of the stratosphere associated with changes in ultraviolet (UV)  
radiation causing an increase in ozone and associated warming during solar maximum conditions.  
The latter results in changes in the latitudinal distribution of UV heating in the stratosphere which  
25 modifies the Eliassen-Palm flux divergence leading to a reduction of the Brewer-Dobson circulation  
(Kodera and Kuroda, 2002; Kuroda and Kodera, 2002; Kodera and Shibata, 2006). Both (1) and  
(2) operate at the same time increasing the complexity of the system response. An extensive model  
based analysis exploring the different effects and its implications is provided by Rind et al. (2008),  
which clearly demonstrates our current lack of understanding of the details of how each mechanism  
30 operates individually and the impacts of coupled processes. Indeed, Kodera et al. (2008) find that  
CO<sub>2</sub> mediated cooling of the stratosphere produces a tropospheric response through a nonlinear  
interaction with the solar cycle. A review of the current state of understanding of the solar cycle  
influence on climate is given by Gray et al. (2010).

Recently, more attention has been devoted to the effects of upper atmosphere NO<sub>x</sub> and HO<sub>x</sub>  
35 produced from ionization by energetic particle precipitation (EPP) on stratospheric ozone. As with  
UV irradiance, the EPP component of the solar cycle has the potential to influence the tropospheric  
response through dynamical processes in the stratosphere that are sensitive to the ozone distribution  
(Callis et al., 2001; Shindell et al., 1999). Indeed, Seppälä et al. (2009) find a statistically signifi-  
cant correlation of wintertime polar northern hemisphere surface air temperatures and the Ap index  
40 using ERA-40 reanalyses from 1957 to 2002 and ECMWF operational data for subsequent years.

Ionization by energetic particle precipitation in the atmosphere is an ubiquitous feature of the  
Sun-Earth system. The work by Warneck (1972), Swider and Keneshea (1973) and Crutzen et al.  
(1975) pioneered research into influence of energetic particle precipitation on the chemistry of the  
atmosphere through the enhancement of NO<sub>x</sub>. Following this early work, Solomon and Crutzen  
45 (1981) and Solomon et al. (1981, 1983) pointed out a coupling mechanism whereby thermospheric  
NO<sub>x</sub> could affect the stratosphere. The Halogen Occultation Experiment (HALOE) instrument on  
the Upper Atmosphere Research Satellite (UARS), and the subsequent Atmospheric Trace Molecule  
Spectroscopy (ATMOS) and Polar Ozone and Aerosol Measurement (POAM) experiments provided  
observational evidence for EPP associated NO<sub>x</sub> enhancement (Callis et al., 1996; Randall et al.,  
50 1998, 2001; Rinsland et al., 1996; Russell et al., 1984). However, little effort was devoted to the  
inclusion of EPP effects in chemistry climate models partly due to complexity and since they were  
considered to be of secondary importance on climate timescales. This has changed in recent years  
prompted by conclusive observational evidence of significant NO<sub>x</sub> enhancement in the polar regions,  
extending to stratospheric altitudes, during major solar proton events (e.g., Siskind, 2000; Randall  
55 et al., 2001, 2005; Hauchecorne et al., 2005, 2007; Jackman et al., 2005; López-Puertas et al., 2005).  
A number of 1, 2 and 3-dimensional model studies, mostly focused on a particular event and some-

times using measured  $\text{NO}_x$  enhancement to force the model have been conducted since then (for a literature review see Jackman et al., 2008; Reddman et al., 2010).

60 The work of Callis et al. (2001) demonstrates that SPEs are not the only type of EPP that can have a significant impact on ozone in the stratosphere and that auroral electron precipitation also needs to be taken into account.

The main difficulty in implementing energetic particle precipitation forcing in general circulation models is the complexity of the D region ion chemistry. One feasible option is to use parameterizations, relating ionization rates to the production of  $\text{NO}_x$  and  $\text{HO}_x$  (e.g., Jackman et al., 2008).  
65 The inclusion of ionization by energetic particles in global self-consistent chemistry climate models started with the work of Langematz et al. (2005) and Rozanov et al. (2005), and has been done differently in different models. For example, while the WACCM implementation described by Marsh et al. (2007) includes thermospheric  $\text{NO}_x$  chemistry explicitly, it does not account for stratospheric production of  $\text{NO}_x$  and  $\text{HO}_x$  due to penetration of high energy galactic cosmic ray particles (GCR).  
70 The implementation in the HAMMONIA model, as described in Schmidt et al. (2006), includes stratospheric NO production by galactic cosmic rays following Heaps (1978) and has the thermospheric NO production based on the scheme of Huang et al. (1998), with the parameters adjusted to reproduce the Student Nitric Oxide Explorer (SNOE) satellite instrument measurements (Barth et al., 2003).  
75 In the recent EPP studies using the ECHAM5/MESSy CCM low energy electron precipitation is parameterized in terms of the Ap index and solar proton events (SPEs) are included in a comprehensive way via a proton transport model (Baumgaertner et al., 2009, 2010).

$\text{HO}_x$  is relatively short-lived (of the order of days) leading mostly to local effects, while  $\text{NO}_x$  can lead to both short and long term (order of months) catalytic ozone destruction in the middle atmosphere. A comprehensive study of the short, middle and long term effects of large SPEs in the  
80 polar regions has been conducted by Jackman et al. (2008, 2009) involving model and measurements. Ozone destruction in the stratosphere can exceed 10% and last up to 5 months depending of the magnitude of the event. Based on their work it is apparent that CCMs are not able to reproduce all the features found by satellite measurements of atmospheric composition. The reasons for this include the fact that CCMs are not constrained to reproduce the observed meteorology and that there  
85 is uncertainty about the ion and neutral chemistry.

The multi-model studies of solar variability effects described by Austin et al. (2008) and the more recent CCMVal-2 project (Manzini et al., 2010) noted an improvement of CCMs in the tropical stratosphere ozone response to the solar cycle in irradiance compared to observations. This was attributed to use of monthly observed sea surface temperatures and monthly or daily variations in solar  
90 irradiance. However, there are still unresolved issues such as the much weaker temperature variation in the tropical stratosphere around and below 10 hPa in most models. The CCMVal projects did not investigate the role of EPP and it remains unclear what direct and indirect role it plays. In spite of the conclusions of Gray et al. (2010), we believe more process oriented model studies are necessary to

understand the effects of EPP. The solar cycle signal is weak and is difficult to extract over short  
95 periods, such as the UARS record, from the internal variability of the chaotic ocean-atmosphere  
system.

As noted above, there is a growing body of work into the effects of EPP on the middle atmosphere. However, to the best of our knowledge there is no published analysis focused on the global role of EPP, including galactic cosmic rays, coupled with the transient solar cycle evolution of the  
100 atmosphere in a chemistry climate model. Previous studies had fixed solar maximum and minimum  
conditions (Schmidt et al., 2006) or did not include GCR (Marsh et al., 2007). The modulation of  
the solar irradiance cycle impact on the stratosphere by EPP is the focus of the work presented here.

We conduct pseudo-timeslice ensemble simulations, which include the solar cycle irradiance  
variation alone and those that also include EPP, using the Canadian Middle Atmosphere Model  
105 (CMAM). CMAM is a chemistry climate model which has been modified to include the solar ir-  
radiance cycle in the solar heating and photolysis rates as described below. Three types of EPP  
were included in the model: auroral electrons, SPEs and GCR. This is a process study where we  
deliberately do not allow for interannual SST variation to reduce the uncertainty in the response.  
A significant part of the interdecadal variability in climate model simulations originates from the  
110 low frequency variation of ocean temperatures. In this study we hope to reduce any aliasing of  
chaotic climate variability onto the solar cycle signal. Also, the solar cycle signal in SSTs is rather  
weak (e.g. Roy and Haigh, 2010) so it is not self-evident that EPP and solar irradiance cycle changes  
in stratospheric composition play a secondary role in the stratospheric response. At the same time,  
it should be recognized that the comparison of the results of this study with observations is limited  
115 since not all processes are included and therefore mostly qualitative.

The EPP effect on the model chemistry is related to the amount of energy deposition, and hence  
ionization, which can be converted into production of atomic nitrogen (Porter et al., 1976) and HO<sub>x</sub>  
(Solomon and Crutzen, 1981). For aurora and SPEs, the vertical profile of the energy deposition  
is inferred from electron and proton fluxes, observed in low earth orbit and in geostationary orbit,  
120 respectively. For GCR we use the Usoskin and Kovaltsov (2006) parameterization for ionization,  
which is also based on observations. More details of the model and EPP parameterizations are given  
in the next section.

## 2 Description of the model and simulations

The CMAM version used here has a spectral dynamical core with a triangular truncation of 31  
125 spherical harmonics. There are 71 sigma-pressure hybrid levels extending from the surface to about  
95 km. A non-zonal sponge layer is applied in the upper two pressure scale heights of the model.  
The radiation scheme of the model takes into account processes which are essential in both the  
troposphere and middle atmosphere. CMAM is the middle atmosphere version of the CCCma third

130 generation climate GCM, which includes a comprehensive set of physical processes, including an interactive land surface scheme, deep and shallow convection parameterizations, orographic and non-orographic gravity wave drag parameterizations. A more detailed description of the CMAM model and its climatology is given in Scinocca et al. (2008), Beagley et al. (1997) and Fomichev et al. (2004).

135 The CMAM has a comprehensive middle atmosphere photochemical scheme as well as heterogeneous chemistry on ice and super saturated ternary solution (STS) polar stratospheric clouds (PSCs) (de Grandpré et al., 1997, 2000) which can capture  $\text{NO}_x$  and  $\text{HO}_x$  production and decay, as well as interaction with chlorine and bromine chemistry (Melo et al., 2008; Brohede et al., 2008). The heterogeneous chemistry scheme does not include processing on nitric acid trihydrate (NAT) particles as well as the associated denitrification. This is not considered to be a major omission as 140 activation of chlorine on NAT is much less effective than on STS and ice, and denitrification typically contributes less than 30% to ozone loss (see Hitchcock et al., 2009, and references therein).

Reddmann et al. (2010) found that NAT was enhanced by about 5% in the Antarctic winter of 2004 and Arctic winter of 2004-2005 when there was significant  $\text{NO}_x$  production by aurora and SPEs. Some underestimation of ozone loss in early spring in response to EPP is expected due to lack of 145 NAT, which typically forms below 25 km. However, as shown in subsequent sections,  $\text{NO}_x$  produced by EPP can destroy ozone over most altitudes in the polar stratosphere and at different times of the year depending on EPP type. So the lack of NAT in the model has a secondary impact on the results.

Intrusions of  $\text{NO}_x$  into the stratosphere are observed to produce a significant enhancement of 150  $\text{HNO}_3$  (Orsolini et al., 2005). The mechanisms by which this occurs are not clear and may be any combination of ion-ion, water ion cluster and heterogeneous reactions on aerosols including possibly sulfate nucleating on meteor smoke (Megner, 2007). For a discussion see Stiller et al. (2005). Since there is no ion chemistry and the sulfate aerosol surface area density is negligible above 30 km in CMAM, conversion of  $\text{N}_2\text{O}_5$  into  $\text{HNO}_3$  in the upper stratosphere winter polar region is underestimated. So our simulations do not produce the strong secondary  $\text{HNO}_3$  maxi- 155 mum in the wake of SPEs or large auroral  $\text{NO}_x$  intrusions such as observed in February 2004 (e.g. Reddmann et al., 2010). Since  $\text{HNO}_3$  is a reservoir species for both  $\text{HO}_x$  and  $\text{NO}_x$ , there may be some overestimation of ozone loss through gas phase catalytic cycles in the upper stratosphere

160 Tropospheric chemistry in this version of CMAM is limited to gas phase reactions. Removal of species is by dry deposition at the surface. There is no chemistry with volatile organic compounds and other aerosols. Surface and lightning emissions of  $\text{NO}_x$  are absent. Nevertheless, we note that the tropospheric ozone values do not deviate significantly from observations (de Grandpré et al., 2000).

165 The model has a reasonable mesospheric and stratospheric climate

(Eyring et al., 2007; Manzini et al., 2010). We used the NAM index method described in McLandress and Shepherd (2009) to determine the major SSW frequency for the runs presented here. They are found to occur  $50 \pm 5\%$  of the time. For these runs major SSWs are important for  $\text{NO}_x$  transport from the upper mesosphere to the stratosphere due to the associated intensification of polar vortex in the mesosphere resulting in more effective polar night confinement (Hauchecorne et al., 2007; Semeniuk et al., 2008; Randall et al., 2009). However, major warmings in the model have highly variable features in different years and are not always effective at organizing  $\text{NO}_x$  transport to the stratosphere. In addition, the major SSWs in the model exhibit highly variable clustering and often occur in successive years as opposed to every other year thereby producing multi-year gaps in occurrence. It should also be noted that free running model SSWs do not occur at the same time as in observations. Analysis of the impact of EPP on the frequency of occurrence of SSWs and their transport characteristics will be presented in a subsequent paper.

For the simulations conducted for this study sea surface temperatures, sea ice and chemical boundary conditions were specified to be repeated 1979 values for the IPCC SRES A1B greenhouse gas (IPCC, 2000) and the WMO Ab halogen (WMO/UNEP, 2003) scenarios. The sea surface temperatures and sea ice were taken from one of the ensemble members of the IPCC AR4 simulations using the coupled ocean-atmosphere version of the CCCma GCM on which CMAM is based. These IPCC AR4 simulations were conducted for the SRES A1B scenario. Any effect of GCR on cloud formation is not included as this is at best a weak effect (e.g., Pallé et al., 2004) and another source of uncertainty to be minimized.

The choice of 1979 conditions for halogens leads to the absence of a deep chemical ozone hole. However, the impact of this on the work presented here is limited. In 1979, there was a dynamical ozone “hole” in the SH polar region in both the observations and the model. The annual mean total column ozone in the SH polar region exhibits a distinct minimum of about 285 DU in the ground based observations (Fioletov et al., 2002) and 250 DU in the model. A maximum of about 340 DU occurs at  $55^\circ$  S. This structure persists from year to year in the model and observations, except that in the case of the latter the increasing halogen burden lowers the total column ozone amount globally. The deep dynamical “hole” in the model is partly a consequence of the late break up of the SH polar vortex. The presence of a chemical ozone hole does not significantly change the intensity of SH polar vortex and the transport characteristics in this region.

Since the  $\text{NO}_x$  and  $\text{HO}_x$  produced by EPP reacts with  $\text{ClO}_x$  to form reservoir species such as  $\text{ClONO}_2$  and  $\text{HOCl}$ , there will be reduced gas phase ozone loss through reactive nitrogen, hydrogen and chlorine catalytic cycles under conditions of increased chlorine which has been the case following 1979. However, during polar night conditions,  $\text{ClO}_x$  amounts are very low above the PSC region where most of the effect of EPP on ozone occurs (e.g. Vogel et al., 2008).

To investigate the impact of individual EPP types single realization runs without solar cycle irradiance variation were conducted over the 1979 through 2006 period for aurora, SPEs, GCR and a

**Table 1.** Brief Description of Simulations

Run	Ensemble members	EPP type	Solar cycle	Section
Reference	3	none	no	4
Aurora	1	Aurora	no	4
SPEs	1	SPEs	no	4
GCR	1	GCR	no	4
Combined	3	Aurora+SPEs+GCR	no	4
Solar	3	none	yes	5
Solar Combined	3	Aurora+SPEs+GCR	yes	5

reference case without EPP. The results are presented in Sect. 4. The role of EPP in the 11-year solar cycle impact on the middle atmosphere was analyzed further with ensemble simulations. A three member ensemble simulation from 1979 through 2006 without EPP but with solar cycle irradiance variation is taken as the reference. A three member ensemble simulation over the same period but with all three types of EPP included together is taken as the perturbation. Effects on the long term mean state as well as variation with the solar cycle are presented in Sect. 5. The various model experiments are summarized in Table 1.

## 2.1 Solar irradiance scheme

The incident solar radiation at the top of the atmosphere varies on different time scales. Variations in the total solar irradiance (TSI), i.e. the spectrally integrated solar irradiance, over the 11-year solar cycle are very small (with an amplitude of approximately 0.1%). However, as noted above, variations in solar irradiance are spectrally dependent and increase considerably with decreasing wavelength in the ultraviolet (UV) part of the spectrum, reaching several percent in ozone absorption bands between 200 and 300 nm and exceeding 10% in the molecular oxygen bands at wavelengths shorter than 200 nm (e.g., Fröhlich and Lean, 2004). To take into account the spectral variability of the solar radiation, both the solar heating and photolysis rates schemes have been modified.

Absorption of solar UV radiation at wavelengths shorter than 300 nm by ozone and molecular oxygen provides the main contribution to the solar heating of the middle atmosphere (e.g., Fomichev, 2009). This means that in order to simulate effects of solar variability in the middle atmosphere, the spectral resolution of the model radiation scheme should be high enough so that it allows for an adequate description of variations in the spectral solar irradiance (SSI) over the solar cycle evolution (e.g., Egorova et al., 2004; Nissen et al., 2007). However, the shortwave radiation scheme of the CMAM exploits only one spectral band between 250 and 690 nm and uses TSI as the solar input for solar heating calculations. This approximation reflects the historical focus of numerical global modeling on the troposphere where absorption of solar UV radiation was thought to play only a very

minor role, given the much lower intensity in the UV spectral region compared to the visible and near-infrared parts of the solar spectrum.

230 In order to properly account for solar input in the current study, a scheme allowing for calculation of variability in solar heating due to variations in SSI at wavelengths shorter than 300 nm has been developed. This scheme takes into account absorption of direct radiation in eight spectral bands between 121 and 300.5 nm (121–122, 125–152, 152–166, 166–175, 175–206, 206–242.5, 242.5–277.5, and 277.5–305.5 nm) and agrees very well with the reference line-by-line calculations  
235 (Fomichev et al., 2010).

Figure 1 presents time series of the solar heating rate deviation from the 1950–2006 mean values at different heights as calculated with the developed scheme. Calculations were done for an equatorial ozone profile and an overhead Sun assuming 24 h illumination with the use of daily varying SSI provided on the SOLARIS website (2008). Changes in solar heating associated with changes in TSI  
240 (blue) and in SSI (green) are shown. As seen from Fig. 1, taking into account variability in TSI only provides a reasonable solar heating signal in the troposphere, where absorption in visible and near-infrared regions dominates the heating rates, but significantly underestimates it in the middle atmosphere. In this case the signal is very small (less than 0.0012 K/day from solar minimum to maximum at 8 km) and has a relatively weak variation with height. With variability in SSI included,  
245 the solar signal considerably increases with height as absorption at shorter wavelengths becomes more important. In this case, the shortwave heating rates between solar minimum and maximum vary by about 0.03, 0.3 and 1 K/day at 32, 48 and 80 km levels, respectively.

To calculate photolysis rates, the CMAM chemistry scheme uses a look-up table (which uses solar  
250 zenith angle, partial ozone column and geometric height as parameters) in which photo-dissociation rates are provided for 165 spectral intervals with a width ranging from 1 to 10 nm between 121 and 852.5 nm. These spectral ranges and spectral resolution are quite sufficient for the purpose of solar variability studies. For the current study, the photolysis scheme has been modified to calculate the look-up table daily reflecting changes in the SSI. Thus, a reasonable solar forcing is provided in the model.

## 255 2.2 EPP parameterization

In these simulations we limit our ionization sources to auroral electrons, solar coronal mass ejection protons and galactic cosmic rays. Electron fluxes are measured by NOAA low earth orbit satellites, proton fluxes are measured by the NOAA GOES geostationary satellites, and galactic cosmic ray intensity is measured by surface neutron monitors.

260 For all EPP types the  $\text{NO}_x$  and  $\text{HO}_x$  production rates were determined from the energy deposition rate,  $E$  ( $\text{eV g}^{-1} \text{s}^{-1}$ ), following the work of Porter et al. (1976). The ionization rate,  $I$  ( $\text{cm}^{-3} \text{s}^{-1}$ ), is given by

$$I = \frac{\rho E}{35.4} \quad (1)$$

where  $\rho$  is the air density in  $\text{g cm}^{-3}$  and the ionization energy is 35.4 eV. The production of  $\text{NO}_x$  is  
265 given by

$$P_{\text{NO}_x} = 1.25I \quad (2)$$

and 45% of  $P_{\text{NO}_x}$  is assumed to produce  $\text{N}(^4\text{S})$  while 55% is assumed to go into  $\text{N}(^2\text{D})$ . The latter  
is added to the production of  $\text{NO}$  and  $\text{O}$  since the reaction of  $\text{N}(^2\text{D})$  with  $\text{O}_2$  to form these products  
is rapid compared to the reaction of  $\text{N}(^4\text{S})$  with  $\text{O}_2$ , which is very temperature dependent. The  
270 production of  $\text{HO}_x$  is given by

$$P_{\text{HO}_x} = aI \quad (3)$$

where  $a(z)$  is a height dependent function that varies from a value of 2 at 40 km to zero above 90 km  
and is an approximation based on the typical variation found in Figure 2 of Solomon et al. (1981).  
The actual production rate has a nearly linear dependence on the logarithm of the ionization rate with  
275 a negative slope depending on altitude. For example, around 75 km it falls from 1.93 to 1.3 as the  
ionization rate increases from 10 to 100,000  $\text{cm}^{-3}\text{s}^{-1}$ . In the lower mesosphere and stratosphere  
the dependence of the production rate on the ionization rate is very small. So the approximation has  
the greatest effect on aurora in our simulations. As shown in later sections, auroral  $\text{HO}_x$  does not  
survive transport into the stratosphere due to its short photochemical lifetime so the impact on ozone  
280 and hence the dynamics of the middle atmosphere is not important.

It is assumed here that  $P_{\text{HO}_x}$  contributes equally to the production of  $\text{H}$  and  $\text{OH}$ . Below 40 km,  
 $a(z)$  is taken to have a constant value of two. This assumption is a limitation since work with a de-  
tailed ion chemistry model (Verronen et al., 2006) indicates that  $\text{HNO}_3$  is an important direct product  
through ion-ion recombination reactions with secondary  $\text{OH}$  production via photodissociation. As  
285 noted by Verronen et al. (2006) assuming a constant  $\text{HO}_x$  production leads to an underestimation of  
 $\text{HO}_x$  production during sunrise and sunset which also affects ozone loss, but only lasts for a short  
period outside polar regions.

Figure 2 shows the time series of the ion pair production rate for the three types of EPP used  
in the model along with the F10.7 solar variability index. Auroral activity maximizes during the  
290 descending stage of the solar cycle. SPEs tend to cluster during solar maximum years when coronal  
activity is enhanced. GCR is anti-correlated with the solar cycle due to the complex heliospheric  
modulation driven by solar magnetic activity.

The vertical profiles of the peak ion pair production rate are shown in Fig. 3 based on the parame-  
terizations described below. Auroral ionization maximizes in the upper mesosphere and above with  
295 a high energy tail that penetrates into the lower mesosphere. SPEs can have maximum ionization  
near the stratopause depending on the energy spectrum of the solar protons (Jackman et al., 2005).  
The GCR profiles peak around 13 km and there is about a factor of two difference between solar  
maximum and minimum conditions.

### 2.2.1 Aurora

300 For aurora the daily energy deposition is inferred from daily composites of electron flux observations from the Medium Energy Proton and Electron Detector (MEPED) instruments on NOAA low earth orbit satellites in the 30–100 keV, 100–300 keV and 300–1000+ keV channels (Seale and Bushnell, 1987). The MEPED data from 1979 through 2006 was used (NOAA/POES website, 2008). Data gaps were filled using the method of singular spectrum analysis (Kondrashov and Ghil, 2006).

305 The lowest energy channel was not used as electrons with this energy are deposited primarily above 100 km and the model lid. The contribution of the region above the model lid to lower altitudes is reduced for three reasons. Firstly, during descent in the lower thermosphere and upper mesosphere region air parcels experience large meridional excursions through wave action. In the polar region of both hemispheres between 80 and 100 km there are wintertime zonal wavenumber 2 planetary waves which propagate eastward (Sandford et al., 2008; Tunbridge and Mitchell, 2009).

310 These waves have peak meridional winds of about 20 m/s and have a two day period but occur for episodes lasting a week or more (Tunbridge and Mitchell, 2009). There are also longer period oscillations peaking above 80 km at high latitudes in the NH. They are eastward and westward traveling and have a zonal wavenumber 1 structure (Pancheva et al., 2008). The period of these waves is pre-

315 dominantly 16 and 23 days and their peak meridional wind amplitudes exceed 20 m/s during major SSW events but are not negligible at other times during winter. They are also very deep with vertical wavelengths in excess of 50 km. It is likely that the SH has analogous disturbances which reflect stratospheric vortex deformation, but with characteristics reflecting the large interhemispheric difference in polar vortex behaviour. When taken together with the fact that the area of the polar night declines with altitude, these waves will contribute to significant loss of  $\text{NO}_x$  through long-distance transport into lower latitudes and photochemical conversion back into  $\text{N}_2$ .

320 Secondly, the descent of air between 100 and 80 km in the winter polar regions is frustrated by the fact that in both hemispheres the zonal wind undergoes a reversal in this layer (e.g., McLandress et al., 2006; Liu et al., 2010). Associated with this wind reversal is a layer where the meridional circulation changes sign and the flow is equatorward with little downward descent rather than poleward and downward. These results are model based but there is observational evidence to support them (e.g., Beagley et al., 2000). The large wave diffusivity at these altitudes to some extent overcomes this large scale transport reversal and drives downgradient tracer fluxes. But there is no simple transport conduit linking the low energy auroral region above 100 km with the mesosphere during winter.

330 The zonal wind reversals also result in a structure that supports barotropic and baroclinic instability and contributes to the growth of large amplitude Rossby wave disturbances (McLandress et al., 2006). As noted above, this reduces the survival of any thermospheric  $\text{NO}_x$  during descent through the MLT.

335 Thirdly, the density decreases exponentially with height. In the vicinity of the mesopause,

between 80 and 90 km, the scale height is about 4 km, so the atmospheric density experiences about a 30-fold reduction between 80 and 100 km. A tracer originating above 100 km will experience a similar or greater reduction factor in mixing ratio during descent to 80 km depending on diffusion. Eddy and wave diffusion increases with height due to amplification of waves on account of density decrease. In the mesosphere the wave energy spectrum has a  $-5/3$  slope (e.g., Koshyk et al., 1999), which indicates a turbulent-like mixing regime. Observations of  $\text{NO}_y$  transport (e.g., Urban et al., 2009; Orsolini et al., 2009) indicate that there is attenuation of mixing ratios in descending plumes of air at the poles. Mixing ratio conservation would require a volumetric collapse of descending tracer plumes.

345 A vertical energy deposition profile was derived using peak flux values from twelve  $30^\circ$  longitudinal sectors at each altitude. The average of these twelve peak electron flux values was used for subsequent calculations. This approach gives an average daily peak intensity that is biased on the high side. However, for the simulations presented here the peak  $\text{NO}_x$  value of  $\sim 5$  ppmv in the polar regions between 80 and 90 km, agrees well with observations (Randall et al., 2009). A more sophisticated statistical model tying observed electron fluxes on orbit tracks to their spatial and temporal distribution in the auroral oval would be more accurate. The dependence of the flux on energy was approximated by a piece-wise exponential fit following Callis et al. (1998). The energy deposition was obtained using the range-energy expression from Gledhill (1973) and the  $80^\circ$ -isotropic energy distribution function from Rees (1989).

355 A parameterized auroral oval was used to obtain a 3-D distribution of electron energy deposition from the vertical profile calculated. The auroral oval is a modified version of the scheme from Holzworth and Meng (1975) based on the formulation of Feldstein (1963). The modification for the auroral horizontal distribution,  $H$ , was as follows:

$$H(\phi, \theta) = \begin{cases} \exp(-((\theta_g(\phi, \theta) - \theta_c)/\delta\theta_p)^2), & \text{if } \theta_g > \theta_c \\ \exp(-((\theta_g(\phi, \theta) - \theta_c)/\delta\theta_e)^2), & \text{if } \theta_g \leq \theta_c \end{cases} \quad (4)$$

$$\theta_c = \theta_e + 0.3(\theta_p - \theta_e)$$

360  $\delta\theta_p = 2(\theta_p - \theta_c)$  (5)

$$\delta\theta_e = (\theta_c - \theta_e)$$

where  $\theta_e$  and  $\theta_p$  are the equatorial and polar corrected geomagnetic latitude limits of the auroral oval, respectively, from the Holzworth and Meng (1975) scheme. This modification was made to improve the realism of the auroral oval distribution when compared to the statistical model of the Space Weather Prediction Center of NOAA (see <http://www.swpc.noaa.gov/pmap/index.html>). The map from geographic longitude ( $\phi$ ) and latitude ( $\theta$ ) on the model grid to corrected geomagnetic latitude ( $\theta_g(\phi, \theta)$ ) was calculated offline using an updated version of the GEOCGM program of Tsyganenko et al. (1987).

Hourly values of the auroral electrojet (AE) index (WDC website, 2008) were used to specify the size of the oval using the relation for the  $Q$  index from Starkov (1994). The orientation of the

370 oval follows the Sun. The parameterized auroral oval resets Q values to six when they exceed this  
number, so that more NO<sub>x</sub> is deposited in the polar night than should be during intense geomagnetic  
storms. In addition, the highest energy electrons are assumed to be distributed in the same auroral  
oval as the lower energy electrons when in fact relativistic electrons are deposited in the sub-auroral  
belt (e.g., Brown, 1966). However, the relativistic electrons account for a small fraction of the NO<sub>x</sub>  
375 production and this limitation of the scheme is not significant.

### 2.2.2 SPEs

For SPEs the daily energy deposition rate vertical profiles were obtained from the dataset of Jackman  
(2006). The horizontal distribution of the energy deposition was approximated by axially symmetric  
caps centered on the geomagnetic poles with a diameter of about 60 degrees (Jackman et al., 2005). A  
380 smooth Gaussian squared transition was assumed between 25° and 45° away from the geomagnetic  
poles with a 5° scaling factor to minimize Gibbs fringing (CMAM uses spectral transport).

### 2.2.3 GCR

Ionization effect of GCR was computed using the CRAC:CRII (Cosmic Ray induced Atmospheric  
Cascade: Application for Cosmic Ray Induced Ionization) model (Usoskin and Kovaltsov, 2006)  
385 extended toward the upper atmosphere (Usoskin et al., 2010). The model is based on the full Monte-  
Carlo simulation of the cosmic ray induced atmospheric cascade and provides computations of the  
ionization rate in 3-D. The accuracy of the model is within 10% in the troposphere and lower strato-  
sphere, and up to a factor of two in the upper atmosphere – mesosphere (Bazilevskaya et al., 2008).  
The temporal variability of the GCR energy spectrum, which is a result of the solar modulation  
390 in the heliosphere, is parameterized via the variable modulation potential, which is computed on a  
monthly basis using the data from the world network of ground-based neutron monitors (Usoskin  
et al., 2005). The final time-dependent ionization rate was computed using the following parameters:  
altitude (quantified via the barometric pressure), geomagnetic latitude (quantified via the geomag-  
netic cutoff rigidity computed in the framework of IGRF-10 model (IAGA/V-MOD website, 2008)  
395 and solar activity (quantified via the modulation potential).

## 3 Regression model

Following the analysis in Austin et al. (2008), we use a linear multiple regression model with first  
order autoregressive, AR(1), error treatment (Tiao et al., 1990) to investigate the solar cycle in key  
model fields. However, instead of subtracting the mean seasonal variation we include annual and  
400 semiannual harmonics. As CMAM simulations do not resolve the QBO and do not contain long  
term variation of total chlorine, aerosols and sea surface temperatures no fitting is done for these  
terms for model output. But QBO, equivalent effective stratospheric chlorine (EESC), aerosol and

El Niño/Southern Oscillation (ENSO) terms are used when fitting the observational data. Thus, for a timeseries of a field, e.g. ozone,  $M$ , we have

$$\begin{aligned}
 405 \quad M = & a_0 + a_1 \sin(\pi \frac{t}{2}) + a_2 \cos(\pi \frac{t}{2}) + \\
 & a_3 \sin(\pi t) + a_4 \cos(\pi t) + bt + \\
 & cS_{F10.7} + d_1 U_{QBO1} + d_2 U_{QBO2} + \\
 & eSAD + fMEI + gEESC + \epsilon
 \end{aligned} \tag{6}$$

where  $t$  is in seasons (three month means),  $S_{F10.7}$  is the F10.7 coronal index normalized by 100, and  
 410  $U_{QBO1}$  and  $U_{QBO2}$  are based on the 30 hPa Singapore winds as in Randel and Wu (2007) and represent two orthogonal QBO wind components. The remaining fitting terms are the sulphate surface area density at 60 hPa, SAD, (Hamill et al., 2006), the Multivariate ENSO index, MEI, (Wolter and Timlin, 1998) and the EESC (Newman et al., 2007).

The height-latitude distributions of the F10.7 regression coefficient,  $c$ , are shown in Sect. 5. This  
 415 coefficient represents the fraction of the timeseries variation that projects onto the F10.7 timeseries. We chose the F10.7 index as a general representation of the solar cycle. The Ap index gives a better fit for the auroral component, as it reflects the variation of the solar wind streams. However, it does not serve the main purpose of this paper, which is to study all main EPP types including SPEs and GCR.

## 420 4 Impact of individual EPP types

The effect of the three EPP types on the long-term composition and dynamics is presented in this section. These runs are single realizations from the 1979 through 2006 period spanned by the EPP data. This 28 year period is too short to have a high confidence level for the dynamical response given dynamical variability. However, they do reveal the distribution of the impact on composition  
 425 and give some idea of the dynamical sensitivity.

### 4.1 Aurora

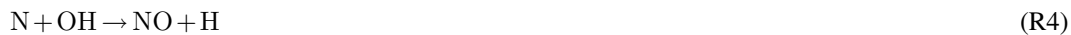
The run mean, December through February mean (DJF) zonal wind, temperature and the transformed Eulerian mean (TEM) mass streamfunction, which represents the Brewer-Dobson circulation (Andrews et al., 1987), for the run with auroral ionization and the reference run (no ionization, no solar  
 430 cycle) are shown in Fig. 4 (left panels). For this figure and other figures with 2-D fields in this paper the Student t-test confidence values of 90% and 95% are marked by dashed and solid black contours, respectively. Both values are plotted to avoid ambiguity as to which regions are statistically significant since the 95% value always encompasses a smaller region than the 90% value. The vertical coordinate in all the figures presented here is geopotential derived geometric height.

435 The change in the NH polar vortex shows a statistically significant increase of its diameter in  
the stratosphere below 30 km. The associated temperature shows a quadrupole structure with sig-  
nificance above 90% only around 50° to 60°N in the lower stratosphere, where it cools, and in  
the stratopause region where it warms. The Brewer-Dobson circulation change has three layers be-  
tween 50° and 80° N with increased strength below 25 km, weakening between 25 and 40 km and  
440 an increase above only to 75° N. However, the Brewer-Dobson circulation change is not statistically  
significant. This highlights the limitations of using the Student t-test for the atmosphere, which has  
non-Gaussian statistics (e.g., Yoden et al., 2002). Of course, the implicit assumption is that changes  
in the zonal wind structure will be reflected in a redistribution of wave drag and hence the diabatic  
circulation. It is possible that there is degeneracy in the wave drag change and the circulation change  
445 is not unique enough to become statistically significant.

The DJF mean, run mean  $\text{NO}_y$ ,  $\text{HO}_x$  and ozone differences for the run with auroral ionization  
and the reference run are shown in Fig. 5 (left panels). There is a large increase of  $\text{NO}_y$  in the winter  
auroral production zone down to about 30 km. We note that above 40 km the  $\text{NO}_y$  is essentially  $\text{NO}_x$ .  
In the summer auroral production zone the increase extends only down to 65 km. The difference in  
the polar regions between the summer and winter is, of course, that the exposure of  $\text{NO}_x$  to sunlight  
in the polar summer results in its cannibalistic destruction, viz.,



which is modulated by reaction with  $\text{O}_2$  and  $\text{OH}$ ,



There is also a significant increase of  $\text{NO}_x$  at all latitudes above 70 km. In the SH summer at middle  
and polar latitudes and between the surface and 20 km,  $\text{NO}_y$  increases by over 5% and this feature is  
most likely a remnant of downward transport of  $\text{NO}_y$  during the previous winter. At these altitudes  
the photochemical lifetime of  $\text{NO}_y$  is long. Also, polar vortex interior air is “fossilized” in the sum-  
450 mertime due to weak mixing (Orsolini, 2001; Orsolini et al., 2003). In the Northern Hemisphere  
during winter, below 40 km, there is a modest decrease of  $\text{NO}_y$  in this latitude range (but not statis-  
tically significant) which may be associated with a strengthening of the Brewer-Dobson circulation.  
Since the disturbed state of the winter NH stratosphere prevents significant transport of  $\text{NO}_y$  into  
this region from above, an increase in transport of low  $\text{NO}_y$  air from the tropics could lead to this  
455 reduction.

The left central panel for  $\text{HO}_x$  shows an increase in both the summer and winter polar mesosphere  
due to the EPP  $\text{HO}_x$  source from water vapour. The largest percentage increase occurs in the winter  
polar regions partly due to the reduced background  $\text{HO}_x$  in winter. Above 70 km at low and middle

latitudes there is no comparable increase of HO<sub>x</sub> as compared to NO<sub>x</sub>. The HO<sub>x</sub> source in this  
 460 region is dominated by photolysis of water vapour. Also, to a lesser extent, the difference is because  
 the photochemical lifetime of HO<sub>x</sub> is shorter (under a day in contrast to 5 days for NO<sub>x</sub>).

In the summer hemisphere, below 40 km there is a decrease in HO<sub>x</sub>. This may be due to changes  
 in the sources and/or sinks of HO<sub>x</sub>. As can be seen in the lowest left panel, ozone has also decreased  
 and so one of the sources of HO<sub>x</sub>, viz. reaction of O(<sup>1</sup>D) (produced from photolysis of ozone) with  
 465 H<sub>2</sub>O, CH<sub>4</sub> and H<sub>2</sub> would decrease. There is also a source from the photolysis of HNO<sub>3</sub>, which has  
 increased in this region (top left panel, NO<sub>y</sub> is primarily HNO<sub>3</sub> at these altitudes). With respect to  
 changes in sinks, the sink via the reaction OH + HNO<sub>3</sub> → H<sub>2</sub>O + NO<sub>3</sub> has increased as well.

The lowest left panel shows that the largest effect on ozone is in the winter polar region above  
 50 km. This reflects that auroral electron ionization occurs in the upper mesosphere polar regions  
 and the HO<sub>x</sub> produced (see middle left panel) leads to reduction of ozone via



and



This effect can also be seen in the summer polar region above 60 km. There is ozone loss of  
 between 2 and 5% between 25 and 40 km in both the winter and summer hemispheres. The additional  
 ozone loss is driven by increases in NO<sub>x</sub> that survived from the previous winter via



There is a transition from O<sub>3</sub> destruction to production in the lowermost stratosphere and tro-  
 posphere (Brasseur and Solomon, 2005). Above roughly 20 km the NO<sub>x</sub> loss cycle (R12–R14)  
 dominates while below the O<sub>3</sub> smog production reactions become important, e.g.



Thus, the increase in  $\text{NO}_x$  below 20 km leads to an increase of ozone. The decrease in the  $\text{HO}_x$  is more than compensated by the increase in  $\text{NO}_x$ .

470 The SH winter, June through August (JJA), dynamical difference compared to the reference run is shown in Figure 6 (left panels). There is a small but statistically significant reduction in the strength of the SH polar vortex (Fig. 6, top left panel) as measured by the reduction in the zonal wind and also by the increase in temperature below 60 km (Fig. 6, middle left panel). The mass streamfunction shows a statistically significant increase poleward of  $60^\circ$  S below 40 km, which is consistent with  
475 the increased temperature and weaker zonal wind above 20 km. Consideration of Eliassen-Palm flux divergence (not shown) shows that increases wave drag, i.e. more negative Eliassen-Palm flux divergence, is responsible for the dynamical changes rather than direct radiative effects from chemical constituent changes. Note that in the SH negative anomalies in the mass streamfunction indicate intensification in contrast to the NH where this applies to positive anomalies due to the change in  
480 sign of the Coriolis parameter at the equator. It is also notable that the Brewer-Dobson circulation change in the SH is hemispheric in scale, as in the NH, in spite of the fact that the ionization impact on composition occurs at high latitudes (see Figs. 5 and 7). The tropospheric response is opposite in sign compared to the NH and statistically significant.

There is an equatorward shift in the extratropical jet with a weakening in middle latitudes and  
485 intensification around  $30^\circ$  S. A possible explanation for this feature can be inferred from the work of Polvani and Kushner (2002). They demonstrated using a mechanistic model that as the stratospheric polar vortex weakens, the subtropical jet moves equatorward. There was no threshold behaviour in the response, so it is plausible that their results apply to the weak changes seen here.

Figure 7 (left panels) shows the atmospheric chemical difference for the SH winter, JJA. The re-  
490 sponse reflects differences in transport between the two hemisphere. For example, the penetration of extra  $\text{NO}_x$  in the SH polar winter is more contained within the vortex than for DJF in the NH. In addition, the increase and penetration in the SH winter extends to 30 km for an 80% change compared to 45 km in the NH winter. The SH summer  $\text{NO}_x$  is higher than for NH summer, which reflects the higher amounts in SH at the end of winter compared to the NH.

495 The NH polar vortex tends to be weaker and more disturbed compared to the SH vortex due to hemispheric differences in planetary wave forcing (Andrews et al., 1987). So perturbations associated with composition changes, unless they are large, are not likely to alter the NH state significantly. As noted above, the more disturbed NH vortex results in increased destruction of auroral  $\text{NO}_x$  by exposure to sunlight during descent as air parcels are transported out of the polar night by planetary  
500 wave induced mixing and vortex deformation. So the chemical impact on dynamics is more limited in the NH compared to the SH.

As expected, there is an increase in  $\text{HO}_x$  in the SH winter polar region above 50 km as a result of EPP and the small background  $\text{HO}_x$  in the reference run. There is also a small enhancement in the NH summer polar region. In the NH winter (Fig. 5, left panels), there is a 5% decrease in

505 HO<sub>x</sub> in mid-latitudes between 50 and 70 km and 30° to 75°N (Fig. 5, middle left panel). Another region of decrease in the NH winter occurs between 30 and 40 km. For the SH winter, the decrease has strengthened and also has become more extensive in the stratosphere extending below 20 km (Fig. 7, middle left panel). Above 60 km, HO<sub>x</sub> is produced by photolysis of H<sub>2</sub>O. Below 60 km it is largely through reaction of O(<sup>1</sup>D) with H<sub>2</sub>O, CH<sub>4</sub> and H<sub>2</sub>. This would suggest that O(<sup>1</sup>D) has decreased in the high latitude stratosphere and lower mesosphere, and to some extent this is reflected by the reduction of ozone in polar regions in SH winter. Whereas there is a substantial decrease in HO<sub>x</sub> in the SH winter between 10 and 40 km, there is a much smaller decrease of HO<sub>x</sub> in this altitude range in the NH winter polar regions. The loss of HO<sub>x</sub> in the winter polar region in the stratosphere is due to reaction with the additional NO<sub>x</sub> transported from the upper mesosphere.

515 The ozone decrease in both the NH and SH polar vortex (Figs. 5 and 7, lower left panels) is caused in the upper regions by HO<sub>x</sub> increases while in the lower regions it is due to increased NO<sub>x</sub> since HO<sub>x</sub> does not survive transport from the mesosphere into the stratosphere. Below 20 km at all latitudes of the SH in JJA there are regions of enhanced ozone with peak significance values above 90% but less than 95% in most regions. These increases in ozone are compatible with the increase of NO<sub>x</sub> produced by aurora of which a fraction is transported to the atmospheric layer below 20 km and the smog reactions noted above. In addition, there is increased transport of O<sub>3</sub> into the lowermost stratosphere and troposphere by the enhanced Brewer-Dobson circulation in the SH (Fig. 6, bottom left panel). It should be noted that these figures are showing percentage differences which can be large due to the typically low ozone values in the troposphere. So even if the ozone anomaly near the pole above 15 km is negative due to chemical loss, it can be positive in the troposphere due to increased transport.

525

## 4.2 SPEs

The DJF change in the polar vortex shows an increase in diameter in the stratosphere as in the case of aurora (Fig. 4, top middle panel). However, the change is only statistically significant below 25 km.

530 There is also a cooling in the lower stratosphere between 30° and 70° N. The Brewer-Dobson circulation response has a three layer structure similar to that with aurora, except the middle layer corresponding to reduced strength is more intense and is statistically significant between 30 and 40 km poleward of 60° N. In contrast to the auroral response, there is a statistically significant poleward shift of the tropospheric jet structure, with weakening in the subtropics and intensification in middle latitudes. Unlike in the SH winter for aurora and SPEs (see below), this tropospheric zonal wind change does not appear to follow the pattern identified by Polvani and Kushner (2002). However, the structure of the stratospheric polar vortex change is more complex and less statistically significant. So it is not immediately apparent which regions are key mediating the stratosphere-troposphere coupling.

535

540 Figure 5 (middle panels) shows the differences in NO<sub>y</sub>, HO<sub>x</sub> and ozone for SPEs in DJF. The

SPEs  $\text{NO}_x$  response pattern is similar to, but much weaker, than that of the auroral case for the mesosphere. Even though there is more ionization produced by individual SPEs in the upper stratosphere and lower mesosphere during each event, it is sporadic and averages out to similar or lower values over the duration of the simulation. In addition, the SPEs  $\text{NO}_x$  is formed lower in the atmosphere and so a given amount created will appear with a lower mixing ratio near the stratopause as compared to the mesopause. The low values of  $\text{NO}_x$  above 70 km in the NH are due to both downward transport from the lower thermosphere where the model lid boundary condition is 1 ppmv, and the fact that SPEs ionization peaks around 60 km so there is much less ionization above 70 km compared to aurora. The higher values of  $\text{NO}_x$  above 70 km in the summer hemisphere (here the NH) are due to the meridional circulation pattern. There is upwelling in the summer polar regions, which lofts the  $\text{NO}_x$  in the mesosphere with transport above the mesopause. An  $\text{NO}_y$  increase between 2 and 7% is present in the SH from the surface to 40 km. There is some accumulation above the extratropical tropopause as with the case of aurora. Between 15 and 25 km in the SH polar region the response is negative but with no statistical confidence. This suggests a high level of variability in this region for this season which is likely due to dynamical processes. There is evanescent penetration of Rossby waves above the summertime zero zonal wind line that can extend as high as 25 km in addition to significant generation of orographic gravity waves by the extreme Antarctic topography (Andrews et al., 1987).

The SPEs  $\text{HO}_x$  response shows an increase in the polar lower mesosphere and upper stratosphere since it is being produced in this region in contrast to the case with aurora, where it is produced above 60 km and does not survive transport into the stratosphere. Below 40 km there is a decrease in  $\text{HO}_x$  through reaction of OH with  $\text{HNO}_3$ , which has been augmented. There is also a reduction in ozone, the source of  $\text{O}(^1\text{D})$  (and thus  $\text{HO}_x$ ), in this region. There is a large negative correlation between the distribution of the  $\text{NO}_y$  and  $\text{HO}_x$  anomalies between 20 and 40 km in high latitudes.

The ozone response is concentrated in the polar regions as for the auroral case. As expected from the intermittency of SPEs the response is weaker but the difference is not large compared to the impact of aurora. There is a roughly 3% decrease near the winter pole around 30 km. As with the auroral case, there is a similar reduction near the summer pole at this height. However, SPEs occur during both summer and winter producing in situ effects not dependent on transport from the upper mesosphere requiring a polar vortex. So this feature is not simply a memory from the previous winter and reflects a summertime contribution from SPEs. In the troposphere, there is an increase of ozone which could be due to increased  $\text{NO}_x$  but the effects of an increased Brewer-Dobson circulation could also be important. However, the changes are not statistically significant.

From the difference plots in Fig. 6 (middle panels) it can be seen that the JJA SH polar vortex is weakened in high latitudes and also becomes broader judging by the larger increase in the zonal wind equatorward of  $60^\circ$  S. The peak negative zonal wind anomaly is comparable to the auroral case. However, the temperature change is weaker and not statistically significant near the pole but

is statistically significant in middle latitudes between 20 and 40 km. There is also a warming in the tropics not present in the auroral case in this layer. It is also not statistically significant. This middle  
580 latitude cooling and tropical warming reflects the weakening of the residual circulation in middle and low latitudes in this layer of the stratosphere (Fig. 6, lower middle panel). The Brewer-Dobson circulation shows an intensification similar to the auroral case in high latitudes below 40 km with some statistical significance below 30 km. There is also a statistically significant weakening of the circulation between 55 and 65 km. This dynamical pattern is the classical response to a localized  
585 wave drag change consisting of a quadrupole temperature anomaly accompanied by a vertical dipolar mass streamfunction anomaly (Haynes et al., 1991). In the troposphere there is a zonal circulation anomaly that resembles the case with aurora and is opposite in sign to DJF.

For JJA  $\text{NO}_y$  and  $\text{HO}_x$  changes (Fig. 7, middle panels) the response is almost the mirror of DJF changes (Fig. 5, middle panels). For JJA, the ozone impact is not as pronounced as for the case of  
590 aurora and is only statistically significant between 20 and 30 km (cf. lower middle and lower left panels of Fig. 7). This reflects the fact that the SPEs are sporadic. It also suggests that the containment properties of the stronger SH polar vortex for  $\text{NO}_x$  produced by SPEs are less important. SPEs  $\text{NO}_x$  production occurs in the lower mesosphere and upper stratosphere and is at lower altitudes compared to aurora so that  $\text{NO}_x$  does not have to survive transport from the upper mesosphere. The  
595 JJA vortex response (Fig. 6, top middle panel) suggests that ozone perturbations of a few percent in the polar region between 20 and 30 km can both induce a weakening of the strength and an increase of the diameter of the SH polar vortex above 25 km.

Vortex variability does play a role in the SPEs case as can be seen by the absence of a significant ozone loss in the NH summer: any  $\text{NO}_x$  produced during the previous winter at higher altitudes  
600 experiences greater loss compared to the SH. Between the tropopause and 25 km during DJF in the SH there is an ozone increase of 3 to 10% which is statistically significant at the 80% confidence level (contours not shown). At these heights this increase is likely due to the smog reactions on account of the  $\text{NO}_x$  increase (about 5%), which more than balances the  $\text{HO}_x$  decrease. This summertime ozone increase is smaller in scale in the NH.

### 605 4.3 GCR

The DJF change in the dynamics induced by GCR is different compared to aurora and SPEs (Fig. 4, right panels). There is some increase of the polar vortex diameter below 30 km but it is not statistically significant. There is no warming near the pole below this altitude as in the other two cases, albeit non-significant. The structure of the Brewer-Dobson circulation change is  
610 quite different, with a general weakening in the NH stratosphere. Between  $30^\circ$  and  $70^\circ$  N in lowermost stratosphere and upper troposphere there is a statistically significant temperature change that resembles the SPEs case and which is associated with a poleward shift of the tropospheric jet in the same region. As with the other two EPP types, the stratospheric effect is obscured by NH vor-

615 tex variability. Yet there is a coherent response in the troposphere. Assuming the Student t-test is good enough to identify any coherent structure in the stratosphere, if one existed, this suggests that different stratospheric states produce similar tropospheric dynamical changes.

620 For the stable SH polar vortex regime the impact of GCR is pronounced as opposed to the NH winter. The dynamical response in JJA shows some similarities to the other two EPP types (Fig. 6, right panels). The polar vortex weakens to a similar degree between 60° S and 80° S above 30 km and this feature is statistically significant. But the reduction is not associated with a vortex diameter increase and there is a weakening in middle and low latitudes as well. The temperature change in the SH reaches lower latitudes and it appears that the wave drag change is broader meridionally compared to the auroral and SPEs cases. The GCR temperature change is most similar to that produced by 625 the stratosphere. The residual circulation intensification in the SH extends over the depth of the stratosphere with a 95% confidence region between the tropopause and 40 km poleward of 60° S. GCR is producing a change of the same sign in wave drag over a broader latitude span in spite of being a weaker source of ionization than the other two types of EPP. As shown below, the GCR effect on ozone is not confined to the polar regions or low altitudes. In the troposphere, there is a 630 statistically significant change in the zonal jet structure that is similar to the case of aurora and SPEs and is of opposite sign to the DJF response in the NH hemisphere. It appears to be due to weakening of the stratospheric polar vortex, as with the other two EPP types.

The DJF and JJA chemical response to GCR is shown in the right panels of Fig. 5 and Fig. 7, respectively. Due to the low altitude and broader latitude span of GCR energy deposition, the ozone 635 impact is quite different from aurora and SPEs. Since GCR peaks around 13 km with a significant tropospheric component, there is up to a 40% increase in NO<sub>y</sub> and about a 15% increase in ozone in the troposphere. These values are a reflection of the lack of wet NO<sub>y</sub> removal in the model. However, the additional ozone in the troposphere is very small and rather well mixed so its effect on temperature gradients and hence dynamics is quite limited. Reflecting the fact that there is negligible 640 impact on tropospheric heating rates, there is no change in tropopause height compared to the reference run except for a small increase in the SH polar region (not shown).

The ionization from GCR above 20 km is small, nevertheless there is a statistically significant ozone loss between the pole and 50° S in a roughly 5 km layer centered at 20 km in JJA. No such ozone loss occurs in the winter polar region in DJF, indicating the effect of a more disturbed vortex 645 in the NH winter. However, in the SH summer there is ozone loss in the polar region between 25 and 30 km, which is associated with enhanced NO<sub>x</sub> in this layer. The SH summer polar region exhibits dynamical variability around 20 km which obscures the chemical impact of GCR, much like in the SPEs case.

The situation in the lowermost stratosphere (between the tropopause and 20 km) is more complex 650 since this is the region where the transition from ozone production to ozone loss for additional NO<sub>x</sub>

occurs (see above). There is poleward and downward transport in the stratosphere which pushes down the GCR induced ozone anomaly in the lowermost stratosphere and brings ozone depleted (number density) air from above 20 km. This transport effect can be seen in the difference in the altitude of the ozone increase between the two hemispheres. There is more diabatic descent in the Northern Hemisphere winter compared to the Southern Hemisphere winter (Andrews et al., 1987) 655 so the region of ozone enhancement does not extend as high into the lowermost stratosphere.

There is a roughly 1% drop in ozone in middle and low latitudes between 20 and 30 km in both JJA and DJF where the GCR  $\text{NO}_x$  production acts to destroy ozone. As with the auroral and SPEs cases there is a loss of  $\text{HO}_x$  below 30 km due to interactions with  $\text{NO}_x$  and  $\text{HNO}_3$ . The difference in the SH middle and low latitude zonal wind change associated with GCR is likely due to the distribution 660 of ozone reduction. The ozone loss around 20 km in the SH winter pole region gives rise to a vortex disturbance similar to the other two EPP cases. The loss of ozone between 20 and 30 km at lower latitudes is likely reducing the radiative equilibrium temperature gradient in this layer in fall and early winter and producing weaker westerlies at these latitudes during JJA (changes in the zonal 665 wind due to thermal wind balance at one height propagate to all heights above). As discussed below this alters the Rossby wave transmission into the SH leading to the hemispheric temperature and circulation changes seen in Fig. 6.

#### 4.4 Combined EPP effect

For each of three EPP simulations conducted there is a reduction in the SH polar vortex strength and a warm temperature anomaly in the polar middle SH stratosphere, which satisfies thermal wind 670 balance (Fig. 6). This is likely due to the decrease in ozone in the middle to high latitudes between 20 km and 30 km. As a result, the meridional gradient of the radiative equilibrium temperature is reduced in the polar region from early winter. This modifies the evolution of the polar vortex, which is slightly weaker becoming more prone to Rossby wave penetration and hence additional wave drag 675 (through radiative damping of Rossby waves directly and through redistribution of the wave breaking in the surf zone). The additional Rossby wave drag increases the Brewer-Dobson circulation in the SH winter, which acts to increase dynamical heating in the polar SH and gives rise to the polar warm temperature anomaly. This picture is supported by analysis of monthly fields of Eliassen-Palm flux divergence, streamfunction and zonal wind (not shown). However, it will become apparent in the 680 next subsection, which presents ensemble runs, that there are other response patterns to EPP which do not conform to this picture.

The timing of the ozone impact on the stratospheric circulation for GCR and SPEs is different from that of aurora since the latter depends on descent of  $\text{NO}_x$  from the upper mesosphere. In the case of aurora, the polar vortex and Brewer-Dobson circulation are modified when the polar 685 vortex is established and there is downward descent from the mesosphere. For the continuously acting GCR ionization (as opposed to transport dependent auroral and intermittent SPEs cases) the

ozone reduction in the stratosphere is present through all stages of polar vortex formation and this may explain why it produces a similar dynamical impact to aurora even though the ozone impact is weaker in the critical region between 20 km and 30 km. SPEs can occur at any time of the year so they can influence the vortex evolution from its early onset stage or when it is established, but the impact is large so that the run mean polar vortex response is not negligible. Based on previous work (Jackman et al., 2005, 2009) there is an ozone memory that extends the period of the SPEs impact from several months to over a year below 10 hPa.

To assess the linearity of the addition of the individual EPP effects we compare differences from the reference run for the sum of the individual runs to a run with all three EPP types combined in Figs. 8 and 9. The combined impact on the chemical composition is essentially additive as seen by the similarity of the magnitudes in the top and bottom panels of Fig. 8. However, for the ozone field this is not true at high latitudes in the stratosphere, where the ozone in the combined run is about a third smaller than when the individual runs are summed. So there is some positive feedback on ozone reduction from the dynamics.

The dynamical response (Fig. 9) is not additive since the response for each of the individual EPP types is comparable to the response of all three combined. This results in the larger values in the top panels compared to the bottom panels in Fig. 9. It appears that the ozone reduction between 20 and 30 km is the common factor in the influence of the EPP types on SH polar vortex evolution. The three EPP types also act out of phase. GCR and SPEs are about 180° out of phase with each other and aurora is 90° out of phase with both (Fig. 2). This, together with the fact that the ozone perturbations are small, implies that the ozone reduction with all three types of EPP present is not different by a large factor between 20 and 30 km. So the magnitude of the dynamical perturbation from the ozone loss in this region is comparable for each of the individual EPP simulations and the combined EPP simulation, although the structure differs. This is supported by the weak non-additivity of the ozone field seen in Fig. 8 (right panels), which indicates that the nonlinear dynamical response to the ozone perturbations saturates with a low amplitude as seen in the small change in the zonal winds (less than ±5 m/s) and temperatures (less than ±2 K). The ozone perturbation from the combination of the three EPP types is not sufficiently large to drive the system out of this low amplitude regime.

#### 4.5 Combined EPP ensemble run

In order to get a more quantitative estimate of the sensitivity of the middle atmosphere to EPP, two additional simulations with all three EPP types combined were produced giving a three member ensemble. The reference run was also extended into an ensemble with two more 28-year realizations. The results are shown in Figures 10 and 11.

There is no longer a statistically significant wintertime zonal wind response in both hemispheres (Fig. 10, left panels). However, in the SH the JJA zonal wind below 20 km and in the troposphere

shows a statistically significant difference pattern that resembles the one identified by Polvani and Kushner (2002). This tropospheric change in the zonal wind was apparent in the runs for the individual EPP types as well. In the ensemble run, the SH polar vortex showed some degree of weakening below 30 km in all members. The NH DJF change in the troposphere is showing some significance at the 90% level and is opposite in sign to the SH JJA response, as seen in the individual runs. The NH winter response in the troposphere is difficult to relate to changes in the stratospheric vortex, which is more variable. The ensemble run mean shows the stratospheric NH winter vortex intensifying around 60° N and poleward below 30 km in contrast to the individual runs where it weakened poleward of 60° N below this height. The only common element appears to be a region of cooling in the middle latitude stratosphere below 30 km with a thin layer of warming around the tropopause.

The SH JJA temperature anomaly structure is different from the individual EPP run cases. It is colder between 20 and 40 km and warmer between 40 and 60 km. The individual EPP cases had a warming between 20 and 50 km with a cooling above. However, there is a significant warming between 5 and 15 km in the SH polar region that is associated with the weakening of the SH polar vortex above through thermal wind balance. The Brewer-Dobson circulation undergoes an intensification in the lowermost SH stratosphere which is consistent with the temperature increase. But between 20 and 40 km the Brewer-Dobson circulation weakens at the pole and in middle latitudes (Fig. 10, top right panel). This behaviour is similar to the SPEs case.

In contrast to the dynamical response, the chemical response is statistically significant and consists of a super-position of the chemical patterns from each of the individual EPP types (Fig. 11). This is consistent with the linearity test from Sect. 4.4.

The combined effect of the three particle precipitation types does not increase the significance level since there is no unique response pattern in the middle atmosphere. A comparison of two of the combined EPP ensemble members for JJA is presented in Figs. 12 and 13, showing differences from the ensemble mean reference run. The SH middle atmosphere can respond to combined EPP forcing either through a weakening of the polar vortex, associated with a warming in the polar stratosphere, and more intense Brewer-Dobson circulation (Fig. 12, top panels), or vice versa (Fig. 12, bottom panels). However, the strong vortex case has a rather complicated structure with a weakening of the vortex closer to the pole between 20 and 40 km. This results in a similar zonal wind anomaly pattern for both cases between the surface and 20 km and in agreement with the findings of Polvani and Kushner (2002).

There are differences in the ozone field (Fig. 13, right panels), for the case with a weakened polar vortex (top panel) compared to the strengthened polar vortex case (bottom panel). Higher ozone values are present between 30 and 50 km in middle and low latitudes for the weakened polar vortex case. The two vortex regimes differentiate starting in May (not shown). The differences in the ozone field are not particularly striking, which highlights the sensitivity to initial conditions in the nonlinear dynamics of the atmosphere. However, the results change when the solar cycle in irradiance is

760 included, as addressed in the next section.

## 5 Combined solar variability and EPP ensemble runs

Here we present results of ensemble simulations which include the solar irradiance cycle. Two ensembles of three members each with and without combined EPP were produced. Each ensemble member was 28 years in duration using the same EPP forcings as the runs in the previous section.

765 The ensemble with solar variability only is used as the reference ensemble for the following analysis instead of the reference ensemble used in Sect. 4 which lacks the solar irradiance cycle.

### 5.1 Long-term differences between the ensemble runs

The dynamical run mean, ensemble mean difference between the reference **solar cycle** ensemble average and the **combined solar cycle and** EPP ensemble average is shown in Fig. 14. In JJA the

770 Brewer-Dobson circulation intensifies in the SH middle and low latitudes between 25 and 40 km. This is associated with a cooling of about 0.25 K in the tropics over the same altitude range. By contrast, the Brewer-Dobson circulation weakens in the NH during DJF around 30 km and there is no longer any significant temperature response between 25 and 40 km in the tropics. The SH polar vortex undergoes a small intensification poleward of about 50° S as well as a reduction around 30° S.  
775 In DJF the zonal wind experiences an intensification around 30° N with less statistically significant reduction in the polar region. The age of air (Fig. 15) is reduced by over 1% in most of the stratosphere in both JJA and DJF, which **shows** that there is an overall intensification of tropical upwelling due to EPP.

The above response pattern of the dynamics differs from the case presented in Fig. 10. Without  
780 solar variability, the SH polar vortex weakens between 20 and 40 km in the presence of EPP and there is no cooling in the tropics in JJA. There is no statistically significant zonal wind response in the NH winter stratosphere as well. The difference in the Brewer-Dobson circulation is more striking in the annual mean (Fig. 16). In the presence of solar variability (top panels) there is a long term intensification in the SH, which is reflected in a weakening of the zonal wind. Due to EPP the age  
785 of air decreases by about 1.3% in the middle atmosphere with solar variability compared to 0.8% without (not shown). Thus, it can be inferred that the solar cycle changes the dynamical sensitivity of the atmosphere to EPP.

The  $\text{NO}_y$ ,  $\text{HO}_x$  and ozone run mean, ensemble mean differences are shown in Fig. 17 and are very similar to the runs without the solar cycle discussed in Sect. 4 (compare Fig. 17 with Fig. 11). The  
790 solar cycle variation in the composition of the middle atmosphere is small, so the EPP perturbation is acting on a similar basic state.

The total column ozone difference (Fig. 18) shows a decrease up to 4% in the winter polar regions. In the NH, the ozone column reduction is concentrated between 60° E and 60° W, while in the SH

the reduction occurs at all longitudes. This reflects the more zonally symmetric structure of the SH polar vortex. In the tropics, there is an increase of about 0.3%. The tropical increase is associated with GCR. The positive impact of GCR on total column ozone at high latitudes (not shown) is overwhelmed by the effect of aurora and SPEs. This can also be inferred from Figs. 5 and 7, which show significant reductions in polar ozone above 15 km.

## 5.2 Solar cycle regression analysis

To analyze the solar cycle effect for runs with and without EPP, we regress the results of the ensemble runs against the F10.7 index. Use of this index is motivated by the fact that previous studies have been based on it (e.g., Austin et al., 2008) and that it captures the overall evolution of the solar cycle. The Ap index is more appropriate for aurora as it reflects geomagnetic activity but it does not suit GCR or SPEs.

### 5.2.1 Latitude-altitude response

The F10.7 index annual mean regression coefficient for zonal mean temperature, ozone, zonal wind, TEM mass streamfunction, Eliassen-Palm flux divergence, age of air and water vapour is shown in Figs. 19–21. Without EPP there is a warm temperature anomaly in the SH polar stratosphere with an associated reduction in the strength of the SH polar vortex (Fig. 19, top panels). The weaker vortex facilitates a Brewer-Dobson circulation increase (Fig. 20, top left) due to additional wave drag (Fig. 20, top right). However, the statistically significant region is below 25 km. The SH warm temperature anomaly appears to be due to the ozone buildup in this region (Fig. 21, top middle). The diabatic circulation increase is hemispheric in scale and results in increased tropical upwelling and some reduction in the age of air in the SH between 20 and 40 km (Fig. 21, top left).

Inclusion of EPP leads to a strikingly different response pattern. The zonal wind variation with the solar cycle in the SH changes sign (Fig. 19, bottom left). This is associated with a weakening of the Brewer-Dobson circulation in the stratosphere (Fig. 20, bottom left), and an increase in the age of air with increased solar activity (Fig. 21, bottom left). In the upper stratosphere in the SH the wave drag now weakens with increased solar activity and this is statistically significant in low and middle latitudes (Fig. 20, bottom right). This explains the statistically significant change in the Brewer-Dobson circulation above 25 km. However, between 20 and 30 km in low and middle latitudes of the SH there is a region where the sign of the wave drag variation with solar activity does not change in the presence of EPP and has a high statistical significance. The origin of this feature is not clear and requires additional analysis. The addition of EPP also leads to a wave drag response in the tropical transition layer (TTL) between 15 and 20 km not seen in the solar cycle ensemble. There is a weakening during solar maximum conditions or, equivalently, a strengthening during solar minimum conditions which occurs in both hemispheres and maximizes between 20° and 30° from the equator. How the high and middle latitude dynamical changes or perhaps GCR effects at lower

latitudes result in a wave drag response in the TTL in both hemispheres is a question that cannot be  
830 answered here but is worthy of additional analysis.

The change in the dynamical response induced by EPP in the SH is due to its effect on high latitude ozone. The statistically significant buildup of ozone with increasing solar activity near the SH pole in the solar cycle ensemble (Fig. 21, top middle) is not present with EPP (Fig. 21, bottom middle). This is reflected in the SH stratosphere temperature  
835 field where the warm anomaly in middle and high latitudes disappears in the presence of EPP (Fig. 19, top right vs. bottom right), in better agreement with observations (Keckhut et al., 2005). The polar ozone buildup with increasing solar activity in the absence of EPP modifies the evolution of the polar vortex during the initial stages of its development so as to make it weaker around 60° S by reducing the meridional temperature gradient. In the presence of EPP there is much  
840 less ozone increase in the sub-polar latitude band and the SH polar vortex intensifies during solar maxima (Fig. 19, bottom left).

In the NH, the high latitude ozone increase with solar activity is also removed by EPP. However, the change is not as extensive as in the SH and there is little difference in the temperature response below 30 km poleward of 40°N (Fig. 19, bottom right). Above 30 km the temperature is decoupled  
845 from the ozone at high latitudes. Presumably, the large difference in polar transport and mixing between the two hemisphere is playing a role.

An interesting effect of inclusion of EPP is the formation of a region with weak ozone response to the solar cycle around 30 km near the equator (Fig. 21, bottom middle). This feature is present in observations (Soukharev and Hood, 2006), although in these simulations it is not as pronounced.  
850 Analysis of the diabatic vertical wind in the tropics (not shown) suggests that there is an increase in the tropical upwelling above 30 km during solar maxima which offsets the buildup of ozone at its mixing ratio peak, which is at 30 km. The enhanced vertical transport is associated with enhanced horizontal transport of ozone to middle latitudes, counteracting the increased photochemical production of ozone.

Another significant feature associated with EPP is the increase in H<sub>2</sub>O around the tropopause level and in the lowermost stratosphere during solar maximum years (Fig. 21, bottom right). This is driven by the warming temperatures in the cold trap region (Fig. 19, bottom middle) in the EPP ensemble. Without EPP there is a cooling in the TTL (Fig. 19, top middle). The source of the TTL temperature variation with the solar cycle and EPP is the increased Brewer-Dobson circulation during solar minimum years. The presence of a positive ozone anomaly in the TTL region is consistent  
860 with reduced upwelling. Partly, this is related to the large, positive vertical gradient of ozone in this region. But also, vertical upwelling is associated with horizontal transport so a weakening of the Brewer-Dobson circulation reduces the loss of ozone to middle latitudes. The H<sub>2</sub>O increase itself leads to additional radiative warming in the TTL. The relative warming of the TTL during solar  
865 maximum years is not associated with enhanced GCR ozone production since it is in the minimum

stage of its cycle when the associated ozone production below 20 km is the lowest.

### 5.2.2 Temporal and spatial profiles

Here the two solar variability ensembles are compared for zonal and global mean total column ozone and tropical mean vertical profiles of the fields presented in the previous subsection.

870 The annual mean, global mean total column ozone variation due to the solar cycle is shown in Fig. 22. EPP can offset some of the solar cycle variation, as seen during the solar maximum around 1990. The observed total column was also relatively lower during this solar maximum. The EESC term should have removed most of the long term variation due to halogen loading so this must be due to other processes. The activity of SPEs combined with aurora was highest during the peak of  
875 the 1990 solar maximum (see Fig. 2). This is reflected in an increased total column of  $\text{NO}_y$  (not shown) which contributes to the reduction of ozone.

A major difference between the model results and observations is the range of global mean total ozone column variation with the solar cycle. Observations range from -6 to 5 DU but the model ranges from -4 to 3 DU. There is much more inter-annual variation in the observations which suggests that some of the difference is dynamical. Due to lack of inter-annual SST variation in the  
880 model it has less variability compared to observations. If a 1-2-1 filter is applied to the observed global mean total column ozone data, across years but keeping the month of the year fixed, then the range becomes -5 to 4 DU.

Figure 23 presents the zonal mean total column ozone variation with latitude. The high latitude  
885 effect of EPP is most apparent in the SH where the maximum in total column ozone variation is greatly reduced and agrees much better with ground based observations (Fioletov et al., 2002, latest data provided courtesy of V. Fioletov). In the NH the variation is underestimated in the model since the model NH polar vortex is too leaky compared to the real atmosphere. For a discussion of Arctic vortex transport isolation see Müller et al. (2005). However, the version of CMAM used in the  
890 present study has a vertical diffusion on tracers that is ten times smaller than in the version discussed in this reference. A comparison of CMAM and other models in terms of transport and dynamics is given in Butchart et al. (2010) and Neu et al. (2010).

Comparing to other models from the CCMVal-1 intercomparison (see Fig. 8 in Austin et al., 2008), the high latitude response in the SH is too large for  
895 most models without EPP. Those models without EPP which lie closer to observations have a much higher variability in the response compared to the results presented here. The WACCM response in this region is similar to the CMAM solar variability ensemble with EPP (Fig. 23, blue curve). This indicates that EPP is an important factor in the high latitude SH ozone solar cycle variation.

Figure 24 (top left) compares the ozone regression coefficient averaged from  $25^\circ\text{S}$  to  $25^\circ\text{N}$  for  
900 the two solar variability ensemble runs and satellite observations (McLinden et al., 2009). As noted above, the model has an ozone solar cycle response minimum around 30 km with EPP. It is not as

deep as in the observations but similar to other models even though we do not have SST imposed variability (Austin et al., 2008). The model study of Matthes et al. (2010) identifies the QBO as an important factor in the tropical stratosphere below 10 hPa for the solar cycle response of ozone. During solar maxima, QBO east phases are associated with enhanced ozone whereas QBO west phases have reduced ozone due to differences in the Brewer-Dobson circulation. However, the origin of the ozone response minimum seen in observations at 10 hPa remains unexplained.

An important source of solar cycle variability that is missing in models without GCR occurs in the tropics, namely the catalytic gas phase destruction via  $\text{NO}_x$  between 20 and 30 km. Values of ozone in this layer of the tropics are lower during solar minima due to increased GCR activity compared to solar maxima. This amplifies the solar cycle ozone variation in this layer. The model ozone response in this layer at low latitudes is statistically significant.

The ozone solar cycle response minimum around 30 km is made more apparent in the presence of EPP due to the direct chemical effect of GCR and the indirect effect of the three types of EPP on dynamics. There are changes in tropical upwelling and its vertical structure, which involve and intensification of the upwelling at and above 30 km during solar maxima (not shown). In spite of the fact that the direct effect of aurora and SPEs on the tropics is limited due to the high latitude confinement of  $\text{NO}_x$  production, the polar vortex perturbations have a global Brewer-Dobson circulation impact that acts to magnify the tropical signal of EPP.

The difference between the two ensembles is highlighted further in the remaining panels of Fig. 24. EPP increases the temperature in the stratosphere tropics due to the reduction in the strength of the Brewer-Dobson circulation during solar maxima relative to solar minima. Below 10 hPa there is much better agreement with observations from the SSU and MSU instruments (Fig. 24, top right). We use channels MSU4, SSU15X, SSU25, SSU26, SSU36X and SSU47X (see caveats in Randel et al., 2009). In our simulations the temperature minimum around 10 hPa is absent without EPP and when it is included, the minimum is not as deep as in models with QBO and variable SSTs (Austin et al., 2008; SPARC CCMVal, 2010). The model average between 10 and 30 hPa is significantly below observations in both CCMVal intercomparisons.

The weakening of the Brewer-Dobson circulation during solar maxima leads to an increase in the age of air (Fig. 24, bottom left). The warming of the TTL in the EPP ensemble results in an increase in the water vapour entering the stratosphere (Fig. 24, bottom right). The inclusion of the solar cycle in most models analyzed by Austin et al. (2008) did not result in any systematic increase in water vapour variation below 20 km (see their Fig. 13) as in our results. However, the only model with upper atmosphere EPP included in addition to the solar cycle, WACCM (Marsh et al., 2007), did have a variation of 1.5%  $\text{H}_2\text{O}$  per 100 units F10.7 at 20 km.

The tropical mean age of air does not show any significant solar cycle dependence in the ensemble without EPP. This differs from the results shown in Fig. 14 of Austin et al. (2008). The solar variability without EPP ensemble had two members opposing the third giving an insignificant response

in the mean. It is possible that three ensemble members is not enough. However, this different behaviour between ensemble members indicates that the dynamical response is not unique. This may no longer be the case if observed or interactive SSTs were used in the model, in which case they may force the middle atmosphere into a response pattern where the age of air increases from solar minimum to solar maximum.

## 6 Discussion and conclusions

The results of our simulations show that addition of EPP to a chemistry climate model makes significant and persistent changes in the natural state of the middle atmosphere. In particular, both aurora and SPEs produce annual mean reductions of ozone in the polar regions of the stratosphere in the 3–10% range depending on location. This is in spite of the fact that auroral ionization peaks above 70 km and SPEs are very intermittent and is consistent with the results of previous studies (Callis et al., 1996; Jackman et al., 2009). There is comparable ozone loss in winter and summer in the polar regions between 20 and 30 km. The  $\text{NO}_y$  produced by EPP survives following the break up of the polar vortex (Orsolini et al., 2003) and continues to destroy ozone catalytically. GCR induces a 1% ozone loss in middle latitudes between 20 and 30 km in addition to indirect ozone loss in this region due to transport of ozone depleted air in the polar vortices and mixing into lower latitudes. These chemical effects of EPP translate into dynamical effects due to the importance of ozone for radiative transfer.

GCR increases  $\text{NO}_y$  by over 10% in the lowermost stratosphere. The  $\text{NO}_y$  of CMAM and other models in this region is lower than in observations (Brohede et al., 2008). So this EPP source together with aurora and SPEs helps to explain part of the deficit.

The long-term mean effect of EPP in the simulations with transient solar forcing presented here is to increase the Brewer-Dobson circulation and tropical upwelling. This reduces the age of air by 1 to 2% in the middle and upper stratosphere. The Brewer-Dobson circulation response varies with the solar cycle; it is weaker during solar maximum years compared to solar minimum years. This behaviour is tied to the EPP modification of the polar vortices through the change in high latitude ozone and hence the radiative equilibrium temperature around the terminator. A reduced meridional gradient of the radiative equilibrium temperature in the 60° to 80° latitude region leads to a slightly weaker polar vortex and hence more Rossby wave penetration which can be explained by the Charney-Drazin criterion (Andrews et al., 1987). This results in more Rossby wave drag in the stratosphere (especially the SH) and thus a stronger Brewer-Dobson circulation. However, the details of this process are subtle and the simulations with combined EPP excluding the solar cycle (Sect. 4) show that the dynamical response can be in the opposite sense as well (weaker Brewer-Dobson circulation and stronger polar vortex).

The regression analysis shows that EPP has a significant impact on the SH zonal wind variation

with the solar cycle. Without EPP the zonal wind becomes weaker during solar maximum years, 975 which does not fit in the idealized picture of Kodera and Kuroda (2002). EPP removes this disagreement. In the NH, the EPP does not alter the basic response of the polar vortex to the solar cycle in the model since it is in a more disturbed regime compared to the SH and the impact of EPP on the ozone evolution in the NH is weaker.

The absence of a well developed Antarctic ozone hole with the choice of chemical boundary conditions in the model is likely to be of secondary importance. EPP generated  $\text{NO}_x$  results in some 980 chlorine sequestration in reservoir species and leads to a relative ozone increase below 23 km. However, the ozone increase occurs at too low an altitude to offset most of the loss in the critical region between 20 and 30 km, so the dynamical sensitivity shown here would still be present. Since there is little impact on the transport characteristics of the SH winter circulation, the high latitude ozone 985 anomaly seen in the regression analysis (Fig. 21) would not disappear. This anomaly originates from ozone produced at altitudes higher than the ozone hole. Also, the ozone hole is a temporally limited feature which occurs in Antarctic spring and so is not particularly relevant for the evolution of the SH polar vortex in late fall and winter. Consequently, we believe that without EPP the sensitivity of the SH polar vortex to the solar cycle would still be in the opposite sense as inferred 990 by Kodera and Kuroda (2002).

There is a Brewer-Dobson circulation reduction during solar maximum years compared to solar minimum years due to the intensification of the polar vortices and reduced Rossby wave penetration and associated drag in line with the idealized picture of Kodera and Kuroda (2002). As a result, there is a tropical temperature increase which results from reduced upwelling, and hence reduced adiabatic 995 cooling, in the TTL. The cold trap warms during solar maxima which then leads to extra  $\text{H}_2\text{O}$  in the tropopause and lowermost stratosphere (up to 4%). Analysis of the tropical tropopause height based on the cold point diagnostic (not shown) indicates that there is no significant change in height due to EPP, specifically GCR and its associated ozone increase of about 15% in the troposphere. So tropopause height is not playing a role in the water vapour variation.

1000 The  $\text{H}_2\text{O}$  variation in the TTL region and the lowermost stratosphere will have an effect on the surface temperature through radiative forcing (Solomon et al., 2010). This water vapour variation just above the tropopause may be an additional driver for the solar response at the surface. However, an explicit evaluation would require simulations with an interactive ocean. To the best of our knowledge, this mechanism has not been suggested before. It is not significant without EPP. This 1005 mechanism can affect decadal surface temperature trends reflecting variations in the solar cycle.

A feature of these results, which has been noted before (e.g., Kodera, 2006), is that high latitude changes in Rossby wave drag are associated with tropical circulation changes. This can be seen in the pole to pole change in the age of air. However, the tropical response cannot be explained simply by the non-local nature of the diabatic streamfunction (Eliassen, 1951). Some of the low 1010 latitude Brewer-Dobson circulation variation from solar minima to solar maxima is due to Rossby

wave propagation changes induced by variation of the polar vortices. But there are also sources associated with the subtropical jets such as synoptic scale Rossby waves and mountain wave drag (McLandress and Shepherd, 2009). There is a localized change of Eliassen-Palm flux divergence in the TTL which contributes to the solar cycle variation in temperature (Fig. 20).

1015 Variation of TTL temperatures and tropical ozone is also induced by interannual variation of SSTs (Schmidt, 2010), an effect which is not included in this study. SSTs change the tropopause height as well as the forcing of planetary Rossby waves so they can significantly influence the middle atmosphere circulation (see Rind et al., 2008, and references therein). The results presented here indicate that EPP has a dynamical signature which may mimic that of SSTs for the tropical ozone  
1020 variability. In particular, the solar cycle ozone response minimum around 30 km is made more prominent through the direct chemical effect of GCR on ozone below 30 km and indirect dynamical effect of all EPP types on the Brewer-Dobson circulation. Whether EPP and SSTs act through a similar response mode of the stratosphere and how they interact needs further investigation. However, EPP cannot be ignored as a factor in the tropical solar cycle signal in ozone, temperature and water  
1025 vapour.

*Acknowledgements.* The authors would like to thank the Natural Sciences and Engineering Research Council of Canada, the Canadian Foundation for Climate and Atmospheric Sciences and the Canadian Space Agency for support. Computing for this work was supported by the Canadian Foundation for Infrastructure, the Canadian Space Agency and the Ontario Innovation Trust.

## 1030 References

- Andrews, D. G., Holton, J. R., and Leovy, C. B.: Middle atmosphere dynamics, Academic Press, Toronto, 489 pp., 1987.
- Austin, J., Tourpali, K., Rozanov, E., Akiyoshi, H., Bekki, S., Bodeker, G., Brühl, C., Butchart, N., Chipperfield, M., Deushi, M., Fomichev, V. I., Giorgetta, M. A., Gray, L., Kodera, K., Lott, F., Manzini, E., Marsh, D.,  
1035 Matthes, K., Nagashima, T., Shibata, K., Stolarski, R. S., Struthers, H., and Tian, W.: Coupled chemistry climate model simulations of the solar cycle in ozone and temperature, *J. Geophys. Res.*, 113, D11306, doi:10.1029/2007JD009391, 2008.
- Barth, C. A., Mankoff, K. D., Balley, S. M., and Solomon, S. C.: Global observations of nitric oxide in the thermosphere, *J. Geophys. Res.*, 108, 1027, doi:10.1029/2002JA009458, 2003.
- 1040 Baumgaertner, A. J. G., Jöckel, P., and Brühl, C.: Energetic particle precipitation in ECHAM5/MESSy1 – Part 1: Downward transport of upper atmospheric NO<sub>x</sub> produced by low energy electrons, *Atmos. Chem. Phys.*, 9, 2729–2740, doi:10.5194/acp-9-2729-2009, 2009.
- Baumgaertner, A. J. G., Jöckel, P., Riede, H., Stiller, G., and Funke, B.: Energetic particle precipitation in ECHAM5/MESSy – Part 2: Solar proton events, *Atmos. Chem. Phys.*, 10, 7285–7302, doi:10.5194/acp-10-7285-2010, 2010.  
1045
- Bazilevskaya, G. A., Usoskin, I. G., Flückiger, E. O., Harrison, R. G., Desorgher, L., Bütikofer, R., Krainev, M. B., Makhmutov, V. S., Stozhkov, Y. I., Svirzhevskaya, A. K., Svirzhevsky, N. S., and Kovaltsov, G. A.: Cosmic ray induced ion production in the atmosphere, *Space Sci. Rev.*, 137, 149–173, doi:10.1007/s11214-008-9339-y, 2008.
- 1050 Beagley, S. R., de Grandpré, J., Koshyk, J. N., McFarlane, N. A., and Shepherd, T. G.: Radiative-dynamical climatology of the first-generation Canadian Middle Atmosphere Model, *Atmos.-Ocean*, 35, 293–331, 1997.
- Beagley, S. R., McLandress, C., Fomichev, V. I., and Ward, W. E.: The extended Canadian middle atmosphere model, *Geophys. Res. Lett.*, 27, 2529–2532, doi:10.1029/1999GL011233, 2000.
- Brasseur, G. P. and Solomon, S.: *Aeronomy of the middle atmosphere*, Springer, 644 pp., The Netherlands,  
1055 2005.
- Brohede, S., McLinden, C. A., Haley, C. S., Jonsson, A. I., and Murtagh, D.: Odin stratospheric proxy NO<sub>y</sub> measurements and climatology, *Atmos. Chem. Phys.*, 8, 5731–5754, doi:10.5194/acp-8-5731-2008, 2008.
- Brown, R. R.: Electron precipitation in the auroral zone, *Space Sci. Rev.*, 5, 311–387, doi:10.1007/BF02653249, 1966.
- 1060 Butchart, N., Charlton-Perez, A. J., and Coauthors: Chapter 4: Stratosphere Dynamics, in: SPARC CCMVal Report on the Evaluation of Chemistry-Climate Models, edited by Eyring, V., Shepherd, T. G., and Waugh, D. W., SPARC, Toronto, Ontario, Canada, Tech. Rep. WCRP-132/WMO/TD-1526/SPARC Rep. 5, 2010.
- Callis, L. B., Baker, D., Natarajan, M., Blake, J., Mewaldt, R., Selesnick, R., and Cummings, J.: A 2D model simulation of downward transport of NO<sub>y</sub> into the stratosphere: Effects on the 1994 austral spring O<sub>3</sub> and  
1065 NO<sub>y</sub>, *Geophys. Res. Lett.*, 23, 1905–1908, doi:10.1029/96GL01788, 1996.
- Callis, L. B., Natarajan, M., Lambeth, J. D., and Baker, D. N.: Solar atmospheric coupling by electrons (SOLACE) 2. Calculated stratospheric effects of precipitating electrons, 1978–1988, *J. Geophys. Res.*, 103, 28,421–28,438, doi:10.1029/98JD02407, 1998.
- Callis, L. B., Natarajan, M., and Lambeth, J. D.: Solar-atmosphere coupling by electrons (SOLACE): 3. Com-

- 1070 parisons of simulations and observations, 1979–1997, issues and implications, *J. Geophys. Res.*, 106, 7523–7539, doi:10.1029/2000JD900615, 2001.
- Crutzen, P. J., Isaksen, I. S. A., and Reid, G. C.: Solar proton events: Stratospheric sources of nitric oxide, *Science*, 189, 457–458, 1975.
- de Grandpré, J., Sandilands, J. W., McConnell, J. C., Beagley, S. R., Croteau, P. C., and Danilin, M. Y.:  
 1075 Canadian Middle Atmosphere Model: preliminary results from the chemical transport module, *Atmos.-Ocean*, 35, 385–431, 1997.
- de Grandpré, J., Beagley, S. R., Fomichev, V. I., Griffioen, E., McConnell, J. C., and Medvedev, A. S.: Ozone climatology using interactive chemistry: Results from the Canadian Middle Atmosphere Model, *J. Geophys. Res.*, 105, 26,475–26,491, doi:10.1029/2000JD900427, 2000.
- 1080 Egorova, T., Rozanov, E., Manzini, E., Haberreiter, M., Schmutz, W., Zubov, V., and Peter, T.: Chemical and dynamical response to the 11-year variability of the solar irradiance simulated with a chemistry-climate model, *Geophys. Res. Lett.*, 31, L06119, doi:10.1029/2003GL019294, 2004.
- Eliassen, A.: Slow thermally or frictionally controlled meridional circulation in a circular vortex, *Astrophys. Norv.*, 5, 19–60, 1951.
- 1085 Eyring, V. et al.: Multimodel projections of stratospheric ozone in the 21st century, *J. Geophys. Res.*, 112, D16303, doi:10.1029/2006JD008332, 2007.
- Feldstein, Y. I.: On morphology and auroral and magnetic disturbances at high latitudes, *Geomagn. Aeron.*, 3, 227–239, 1963.
- Fioletov, V. E., Bodeker, G. E., Miller, A. J., McPeters, R. D., and Stolarski, R.: Global and zonal total ozone  
 1090 variations estimated from groundbased and satellite measurements: 1964–2000, *J. Geophys. Res.*, 107, 4647, doi:10.1029/2001JD001350, 2002.
- Fomichev, V. I.: The radiative energy budget of the middle atmosphere and its parameterizations in general circulation models., *J. Atmos. Sol.-Terr. Phys.*, 71, 1577–1585, doi:10.1016/j.jastp.2009.04.007, 2009.
- Fomichev, V. I., Fu, C., de Grandpré, J., Beagley, S. R., Ogibalov, V. P., and McConnell, J. C.: Model thermal  
 1095 response to minor radiative energy sources and sinks in the middle atmosphere, *J. Geophys. Res.*, 109, D19107, doi:10.1029/2004JD004892, 2004.
- Fomichev, V. I., Forster, P. M., and Coauthors: Chapter 3: Radiation, in: SPARC CCMVal Report on the Evaluation of Chemistry-Climate Models, edited by Eyring, V., Shepherd, T. G., and Waugh, D. W., SPARC, Toronto, Ontario, Canada, Tech. Rep. WCRP-132/WMO/TD-1526/SPARC Rep. 5, 2010.
- 1100 Fröhlich, C. and Lean, J.: Solar radiative output and its variability: evidence and mechanisms, *Astron. Astrophys. Rev.*, 12, 273–320, doi:10.1007/s00159-004-0024-1, 2004.
- Gledhill, J. A.: The range-energy relation for 0.1–600 keV electrons, *J. Phys. A: Math. Nucl. Gen.*, 6, 1420–1428, 1973.
- Gray, L. J., Beer, J., Geller, M., Haigh, J. D., Lockwood, M., Matthes, K., Cubasch, U., Fleitmann, D., Harrison,  
 1105 G., Hood, L., Luterbacher, J., Meehl, G. A., Shindell, D., van Geel, B., and White, W.: Solar influences on climate, *Rev. Geophys.*, 48, RG4001, doi:10.1029/2009RG000282, 2010.
- Hamill, P., Brogniez, C., and Coauthors: Chapter 4: Stratospheric aerosol record and climatology, in: Assessment of Stratospheric Aerosol Properties (ASAP), edited by: Thomason, L. and Peter, T., 107–176, SPARC, Toronto, Ontario, Canada, Tech. Rep. WCRP-124/WMO/TD-1295/SPARC Rep. 4, 2006.

- 1110 Hauchecorne, A., Bertaux, J.-L., Dalaudier, F., Cot, C., Lebrun, J.-C., Bekki, S., Marchand, M., Kyrölä, E., Tamminen, J., Sofieva, V., Fussen, D., Vanhellefont, F., d'Andon, O. F., Barrot, G., Mangin, A., Théodore, B., Guirlet, M., Snoeij, P., Koopman, R., de Miguel, L. S., Fraisse, R., and Renard, J.-B.: First simultaneous global measurements of nighttime stratospheric NO<sub>2</sub> and NO<sub>3</sub> observed by Global Ozone Monitoring by Occultation of Stars (GOMOS)/Envisat in 2003, *J. Geophys. Res.*, 110, D18301, doi:10.1029/2004JD005711, 2005.
- 1115 Hauchecorne, A., Bertaux, J.-L., Dalaudier, F., Russell III, J. M., Mlyneczek, M. G., Kyrölä, E., and Fussen, D.: Large increase of NO<sub>2</sub> in the north polar mesosphere in January–February 2004: Evidence of a dynamical origin from GOMOS/ENVISAT and SABER/TIMED data, *Geophys. Res. Lett.*, 34, L03810, doi:10.1029/2006GL027628, 2007.
- 1120 Haynes, P. H., Marks, C. J., McIntyre, M. E., Shepherd, T. G., and Shine, K. P.: On the “downward control” of extratropical diabatic circulations by eddy-induced mean zonal forces, *J. Atmos. Sci.*, 48, 651–678, 1991.
- Heaps, M.: Parameterization of the cosmic ray ion-pair production rate above 18 km, *Planet Space Sci.*, 26, 513–517, 1978.
- Hitchcock, P., Shepherd, T. G., and McLandress, C.: Past and future conditions for polar stratospheric cloud formation simulated by the Canadian Middle Atmosphere Model, *Atmos. Chem. Phys.*, 9, 483–495, doi:10.5194/acp-9-483-2009, 2009.
- 1125 Holzworth, R. H. and Meng, C.-I.: Mathematical representation of the auroral oval, *Geophys. Res. Lett.*, 2, 377–380, doi:10.1029/GL002i009p00377, 1975.
- Huang, T. Y. W., Brasseur, G. P., and Coauthors: Description of the SOCRATES – A chemical dynamical radiative two-dimensional model., Tech. Rep. NCAR/TN-440+EDD, NCAR, Boulder, CO, 94 pp., 1998.
- 1130 IAGA/V-MOD website:<http://www.ngdc.noaa.gov/IAGA/vmod>, 2008.
- IPCC: Special Report on Emission Scenarios, Technical report, Intergovernmental Panel on Climate Change, Cambridge University Press, Cambridge, UK, 599 pp., 2000.
- Jackman, C. H.: Ionization rates for 1963–2005 from solar proton events, [http://www.geo.fu-berlin.de/en/met/ag/strat/forschung/SOLARIS/Input\\_data](http://www.geo.fu-berlin.de/en/met/ag/strat/forschung/SOLARIS/Input_data), unpublished technical note, 2006.
- 1135 Jackman, C. H., DeLand, M. T., Labow, G. J., Fleming, E. L., Weisenstein, D. K., Ko, M. K. W., Sinnhuber, M., Anderson, J., and Russell, J. M.: The influence of the several very large solar proton events in years 2000–2003 on the neutral middle atmosphere, *Adv. Space Res.*, 35, 445–450, 2005.
- Jackman, C. H., Marsh, D. R., Vitt, F. M., Garcia, R. R., Fleming, E. L., Labow, G. J., Randall, C. E., López-Puertas, M., Funke, B., von Clarmann, T., and Stiller, G. P.: Short and medium-term atmospheric constituent effects of very large solar proton events, *Atmos. Chem. Phys.*, 8, 765–785, doi:10.5194/acp-8-765-2008, 2008.
- 1140 Jackman, C. H., Marsh, D. R., Vitt, F. M., Garcia, R. R., Randall, C. E., Fleming, E. L., and Frith, S. M.: Long-term middle atmosphere influence of very large solar proton events, *J. Geophys. Res.*, 114, D11304, doi:10.1029/2008JD011415, 2009.
- 1145 Keckhut, P., Cagnazzo, C., Chanin, M.-L., Claud, C., and Hauchecorne, A.: The 11-year solar-cycle effects on the temperature in the upper-stratosphere and mesosphere: Part I–Assessment of observations, *J. Atmos. Sol.-Terr. Phys.*, 67, doi:10.1016/j.jastp.2005.01.008, 2005.
- Kodera, K.: Influence of stratospheric sudden warming on the equatorial troposphere, *Geophys. Res. Lett.*, 33,

- 1150 L086804, doi:10.1029/2005GL024510, 2006.
- Kodera, K. and Kuroda, Y.: Dynamical response to the solar cycle, *J. Geophys. Res.*, 107, 4749, doi:10.1029/2002JD002224, 2002.
- Kodera, K. and Shibata, K.: Solar influence on the tropical stratosphere and troposphere in the northern summer, *Geophys. Res. Lett.*, 33, L19704, doi:10.1029/2006GL026659, 2006.
- 1155 Kodera, K., Hori, M. E., Yukimoto, S., and Sigmond, M.: Solar modulation of the Northern Hemisphere winter trends and its implications with increasing CO<sub>2</sub>, *Geophys. Res. Lett.*, 35, L03704, doi:10.1029/2007GL031958, 2008.
- Kondrashov, D. and Ghil, M.: Spatio-temporal filling of missing points in geophysical data sets, *Nonlinear Processes Geophys.*, 13, 151–159, doi:10.5194/npg-13-151-2006, 2006.
- 1160 Koshyk, J. N., Boville, B. A., Hamilton, K., Manzini, E., and Shibata, K.: Kinetic energy spectrum of horizontal motions in middle-atmosphere models, *J. Geophys. Res.*, 104, doi:10.1029/1999JD900814, 1999.
- Kuroda, Y. and Kodera, K.: Effect of the solar cycle on the Polar-night jet oscillation, *J. Met. Soc. Japan*, 80, 973–984, 2002.
- Langematz, U., Grenfell, J. L., Matthes, K., Mieth, P., Kunze, M., Steil, B., and Brühl, C.: Chemical effects in 11-year solar cycle simulations with the Freie Universität Berlin Climate Middle Atmosphere Model with online chemistry (FUB-CMAM-CHEM), *Geophys. Res. Lett.*, 32, L13803, doi:10.1029/2005GL022686, 2005.
- 1165 Liu, H.-L., Foster, B. T., Hagan, M. E., McInerney, J. M., Maute, A., Qian, L., Richmond, A. D., Roble, R. G., Solomon, S. C., Garcia, R. R., Kinnison, D., Marsh, D. R., Smith, A. K., Richter, J., Sassi, F., and Oberheide, J.: Thermosphere extension of the Whole Atmosphere Community Climate Model, *J. Geophys. Res.*, 115, A12302, doi:10.1029/2010JA015586, 2010.
- López-Puertas, M., Funke, B., Gil-Lopéz, S., von Clarmann, T., Stiller, G. P., Hopfner, M., Kellmann, S., Fischer, H., and Jackman, C. H.: Observation of NO<sub>x</sub> enhancement and ozone depletion in the Northern and Southern Hemispheres after the October–November 2003 solar proton events, *J. Geophys. Res.*, 110, A09S43, doi:10.1029/2005JA011050, 2005.
- 1175 Manzini, E., Matthes, K., and Coauthors: Chapter 8: Natural Variability of Stratospheric Ozone, in: SPARC CCMVal Report on the Evaluation of Chemistry–Climate Models, edited by Eyring, V., Shepherd, T. G., and Waugh, D. W., SPARC, Toronto, Ontario, Canada, Tech. Rep. WCRP-132/WMO/TD-1526/SPARC Rep. 5, 2010.
- 1180 Marsh, D. R., Garcia, R. R., Kinnison, D. E., Boville, B. A., Sassi, F., Solomon, S. C., and Matthes, K.: Modeling the whole atmosphere response to solar cycle changes in radiative and geomagnetic forcing, *J. Geophys. Res.*, 112, D23306, doi:10.1029/2006JD008306, 2007.
- Matthes, K., Marsh, D. R., Garcia, R. R., Kinnison, D. E., Sassi, F., and Walters, S.: Role of the QBO in modulating the influence of the 11 year solar cycle on the atmosphere using constant forcings, *J. Geophys. Res.*, 115, D18110, doi:10.1029/2009JD013020, 2010.
- 1185 McLandress, C., Ward, W. E., Fomichev, V. I., Semeniuk, K., Beagley, S. R., McFarlane, N. A., and Shepherd, T. G.: Large-scale dynamics of the mesosphere and lower thermosphere: An analysis using the extended Canadian Middle Atmosphere Model, *J. Geophys. Res.*, 111, D17111, doi:10.1029/2005JD006776, 2006.
- McLandress, C. and Shepherd, T. G.: Impact of climate change on stratospheric sudden warmings as simulated

- 1190 by the Canadian Middle Atmosphere Model, *J. Clim.*, 22, 5449–5463, doi:10.1175/2009JCLI3069.1, 2009.
- McLinden, C. A., Tegtmeier, S., and Fioletov, V.: Technical Note: A SAGE-corrected SBUV zonal-mean ozone data set, *Atmos. Chem. Phys.*, 9, 7963–7972, doi:10.5194/acp-9-7963-2009, 2009.
- Megner, L.: Funneling of meteoric material into the polar vortex, in: *Nucleation and Atmospheric Aerosols*, O’Dowd, C. D. and Wagner, P. E. (Eds.), Springer, Netherlands, 860–864, doi:10.1007/978-1-4020-6475-3\_170, 2007.
- 1195 Melo, S. M. L., Blatherwick, R., Davies, J., Fogal, P., de Grandpré, J., McConnell, J. C., McElroy, C. T., McLandress, C., Murcray, F. J., Olson, J. R., Semeniuk, K., Shepherd, T. G., Strong, K., Tarasick, D., and Williams-Rioux, B. J.: Summertime stratospheric processes at northern mid-latitudes: comparisons between MANTRA balloon measurements and the Canadian Middle Atmosphere Model, *Atmos. Chem. Phys.*, 8, 2057–2071, doi:10.5194/acp-8-2057-2008, 2008.
- 1200 Müller, R., Tilmes, S., Konopka, P., Grooß, J.-U., and Jost, H.-J.: Impact of mixing and chemical change on ozone-tracer relations in the polar vortex, *Atmos. Chem. Phys.*, 5, 3139–3151, doi:10.5194/acp-5-3139-2005, 2005.
- Neu, J., Strahan, S., and Coauthors: Chapter 5: Transport, in: *SPARC CCMVal Report on the Evaluation of Chemistry-Climate Models*, edited by Eyring, V., Shepherd, T. G., and Waugh, D. W., SPARC, Toronto, Ontario, Canada, Tech. Rep. WCRP-132/WMO/TD-1526/SPARC Rep. 5, 2010.
- 1205 Newman, P. A., Daniel, J. S., Waugh, D. W., and Nash, E. R.: A new formulation of equivalent effective stratospheric chlorine (EESC), *Atmos. Chem. Phys.*, 7, 4537–4552, doi:10.5194/acp-7-4537-2007, 2007.
- Nissen, K. M., Matthes, K., Langematz, U., and Mayer, B.: Towards a better representation of the solar cycle in general circulation models, *Atmos. Chem. Phys.*, 7, 5391–5400, doi:10.5194/acp-7-5391-2007, 2007.
- 1210 NOAA/POES website: <http://ngdc.noaa.gov/stp/satellite/poes/index.html>, 2008.
- Orsolini, Y. J.: Long-lived tracer patterns in the summer polar stratosphere, *Geophys. Res. Lett.*, 28, 3855–3858, doi:10.1029/2001GL013103, 2001.
- Orsolini, Y. J., Eskes, H., Hansen, G., Hoppe, U.-P., Kylling, A., Kyrö, E., Notholt, J., Van der A, R., and von der Gathen, P.: Summertime low-ozone episodes at northern high latitudes, *Q. J. Roy. Met. Soc.*, 129, 3265–3275, doi:10.1256/qj.02.211, 2003.
- 1215 Orsolini, Y. J., Manney, G. L., Santee M., and Randall, C. E.: An upper stratospheric layer of enhanced HNO<sub>3</sub> following exceptional solar storms, *Geophys. Res. Lett.*, 32, L12S01, doi:10.129/2004GL021588, 2005.
- Orsolini, Y. J., Urban, J., and Murtagh, D. P.: Nitric acid in the stratosphere based on Odin observations from 2001 to 2009 – Part 2: High-altitude polar enhancements, *Atmos. Chem. Phys.*, 9, 7045–7052, doi:10.5194/acp-9-7045-2009, 2009.
- 1220 Pallé, E., Butler, C. J., and O’Brien, K.: The possible connection between ionization in the atmosphere by cosmic rays and low level clouds, *J. Atmos. Sol-Terr. Phys.*, 66, 1779–1790, doi:10.1016/j.jastp.2004.07.041, 2004.
- 1225 Pancheva, D., Mukhtarov, P., Mitchell, N. J., Merzlyakov, E., Smith, A. K., Andonov, B., Singer, W., Hocking, W., Meek, C., Manson, A., and Murayama, Y.: Planetary waves in coupling the stratosphere and mesosphere during the major stratospheric warming in 2003/2004, *J. Geophys. Res.*, 113, D12105, doi:10.1029/2007JD009011, 2008.
- Polvani, L. M. and Kushner, P. J.: Tropospheric response to stratospheric perturbations in relatively simple

- 1230 general circulation model, *Geophys. Res. Lett.*, 29, 1114, doi:10.1029/2001GL014284, 2002.
- Porter, H. S., Jackman, C. H., and Green, A. E. S.: Efficiencies for production of atomic nitrogen and oxygen by relativistic proton impact in air, *J. Chem. Phys.*, 65, 154–167, doi:10.1063/1.432812, 1976.
- Randall, C., Rusch, D., Bevilacqua, R., Hoppel, K., and Lumpe, J.: Polar Ozone and Aerosol Measurement (POAM) II stratospheric NO<sub>2</sub>, 1993–1996, *J. Geophys. Res.*, 103, 28,361–28,371, doi:10.1029/98JD02092, 1235 1998.
- Randall, C. E., Siskind, D. E., and Bevilacqua, R. M.: Stratospheric NO<sub>x</sub> enhancement in the Southern Hemisphere vortex in winter/spring of 2000, *Geophys. Res. Lett.*, 28, 2385–2388, doi:10.1029/2000GL012746, 2001.
- Randall, C. E., Harvey, V. L., Manney, G. L., Orsolini, Y., Codrescu, M., Sioris, C., Brohede, S., Haley, C. S., 1240 Gordley, L. L., Zawodny, J. M., and Russell III, J. M.: Stratospheric effects of energetic particle precipitation in 2003–2004, *Geophys. Res. Lett.*, 32, L05802, doi:10.1029/2004GL022003, 2005.
- Randall, C. E., Harvey, V. L., Siskind, D., France, J., Bernath, P., Boone, C., and Walker, K.: NO<sub>x</sub> descent in the Arctic middle atmosphere in early 2009, *Geophys. Res. Lett.*, 36, L18811, doi:10.1029/2009GL039706, 2009.
- 1245 Randel, W. J. and Wu, F.: A stratospheric ozone profile data set for 1979–2005: Variability, trends, and comparisons with column ozone data, *J. Geophys. Res.*, 112, D06313, doi:10.1029/2006JD007339, 2007.
- Randel, W. J., Shine, K. P., Austin, J., Barnett, J., Claud, C., Gillett, N. P., Keckhut, P., Langematz, U., Lin, R., Long, C., Mears, C., Miller, A., Nash, J., Seidel, D. J., Thompson, D. W. J., Wu, F., and Yoden, S.: An update of observed stratospheric temperature trends, *J. Geophys. Res.*, 114, D02107, doi:10.1029/2008JD010421, 1250 2009.
- Reddmann, T., Ruhnke, R., Versick, S., and Kouker, W.: Modeling disturbed stratospheric chemistry during solar-induced NO<sub>x</sub> enhancements observed with MIPAS/ENVISAT, *J. Geophys. Res.*, 115, D00I11, doi:10.1029/2009JD012569, 2010.
- Rees, M. H.: *Physics and chemistry of the upper atmosphere*, Cambridge University Press, Cambridge, UK, 1255 289 pp., 1989.
- Rind, D., Lean, J., Lerner, J., Lonergan, P., and Leboissitier, A.: Exploring the stratospheric/tropospheric response to solar forcing, *J. Geophys. Res.*, 113, D24103, doi:10.1029/2008JD010114, 2008.
- Rinsland, C. P., Gunson, M. R., Salawitch, R. J., Newchurch, M. J., Zander, R., Abbas, M. M., Abrams, M. C., Manney, G. L., Michelsen, H. A., Chang, A. Y., and Goldman, A.: ATMOS measurements of H<sub>2</sub>O + 2CH<sub>4</sub> and total reactive nitrogen in the November 1994 Antarctic stratosphere: Dehydration and denitrification in the vortex, *Geophys. Res. Lett.*, 23, 2397–2400, doi:10.1029/96GL00048, 1996.
- 1260 Roy, I., and Haigh, J. D.: Solar cycle signals in sea level pressure and sea surface temperature, *Atmos. Chem. Phys.*, 10, 3147–3153, doi:10.5194/acp-10-3147-2010, 2010.
- Rozanov, E., Callis, L., Schlesinger, M., Yang, F., Andronova, N., and Zubov, V.: Atmospheric response to NO<sub>y</sub> source due to energetic electron precipitation, *Geophys. Res. Lett.*, 32, L14811, doi:10.1029/2005GL023041, 1265 2005.
- Russell, J. M., Solomon, S., Gordley, L. L., Remsberg, E. E., and Callis, L. B.: The variability of stratospheric and mesospheric NO<sub>2</sub> in the polar winter night observed by LIMS, *J. Geophys. Res.*, 89, 7267–7275, doi:10.1029/JD089iD05p07267, 1984.

- 1270 Sandford, D. J., Schwartz, M. J., and Mitchell, N. J.: The wintertime two-day wave in the polar stratosphere, mesosphere and lower thermosphere, *Atmos. Chem. Phys.*, 8, 749–755, doi:10.5194/acp-8-749-2008, 2008.
- Schmidt, H.: Numerical simulation of the MLT response to natural and anthropogenic forcing for the period 1960 to 2006, The 6th IAGA/ICMA/CAWSES workshop on Long-Term Changes and Trends in the Atmosphere, NCAR, Boulder, Colorado, USA, 15–18 June, 2010.
- 1275 Schmidt, H., Brasseur, G. P., Charron, M., Manzini, E., Giorgetta, M. A., Diehl, T., Fomichev, V. I., Kinnison, D., Marsh, D., and Walters, S.: The HAMMONIA chemistry climate model: sensitivity to the mesopause region to the 11 years solar cycle and CO<sub>2</sub> doubling, *J. Clim.*, 19, 3903–3931, 2006.
- Scinocca, J. F., McFarlane, N. A., Lazare, M., Li, J., and Plummer D.: Technical note: The CCCma third generation AGCM and its extension into the middle atmosphere, *Atmos. Chem. Phys.*, 8, 7055–7074, doi:10.5194/acp-8-7055-2008, 2008.
- 1280 Seale, R. A. and Bushnell, R. H.: TIROS-N/NOAA A-J space environment monitor subsystem, NOAA technical memorandum ERL SEL:75, National Oceanic and Atmospheric Administration, Environmental Research Laboratories, Space Environment Laboratory, Boulder, Colorado, USA, 1987.
- Semeniuk, K., McConnell, J. C., Jin, J. J., Jarosz, J. R., Boone, C. D., and Bernath, P. F.: N<sub>2</sub>O production by high energy auroral electron precipitation, *J. Geophys. Res.*, 113, D16302, doi:10.1029/2007JD009690, 2008.
- 1285 Seppälä, A., Randall, C. E., Clilverd, M. A., Rozanov, E., and Rodger, C. J.: Geomagnetic activity and polar surface air temperature variability, *J. Geophys. Res.*, 114, A10312, doi:10.1029/2008JA014029, 2009.
- Shindell, D., Rind, D., Balachandran, N., Lean, J., and Lonergan, P.: Solar cycle variability, ozone, and climate, *Science*, 284, 305–308, doi:10.1126/science.284.5412.305, 1999.
- 1290 Siskind, D. E.: On the coupling between middle and upper atmospheric odd nitrogen, in: *Atmospheric Science Across the Stratopause*, *Geophys. Monogr. Ser.*, vol. 123, edited by: Siskind, D. E., Eckermann, S. D., and Summers, M. E., 101–116, AGU, Washington, DC, USA, 2000.
- SOLARIS website: [http://www.geo.fu-berlin.de/en/met/ag/strat/forschung/SOLARIS/Input\\\_data](http://www.geo.fu-berlin.de/en/met/ag/strat/forschung/SOLARIS/Input\_data), 2008.
- 1295 Solomon, S. and Crutzen, P. J.: Analysis of the August 1972 solar proton event including chlorine chemistry, *J. Geophys. Res.*, 86, 1140–1146, doi:10.1029/JC086iC02p01140, 1981.
- Solomon, S., Rusch, D. W., Gerard, J. C., Reid, G. C., and Crutzen, P. J.: The effect of particle precipitation events on the neutral and ion chemistry of the middle atmosphere, 2, Odd hydrogen, *Planet. Space Sci.*, 29, 885–893, doi:10.1016/0032-0633(81)90078-7, 1981.
- 1300 Solomon, S., Reid, G. C., Rusch, D. W., and Thomas, R. J.: Mesospheric ozone depletion during the solar proton event of July 13, 1982, 2, Comparison between theory and measurements, *Geophys. Res. Lett.*, 10, 257–260, 1983.
- Solomon, S., Rosenlof, K. H., Portmann, R. W., Daniel, J. S., Davis, S. M., Sanford, T. J., and Plattner, G.-K.: Contributions of stratospheric water vapor to decadal changes in the rate of global warming, *Science*, 327, 1219–1223, doi:10.1126/science.1182488, 2010.
- 1305 Soukharev, B. E. and Hood, L. L.: Solar cycle variation of stratospheric ozone: Multiple regression analysis of long-term satellite data sets and comparison with models, *J. Geophys. Res.*, 111, D20314, doi:10.1029/2006JD007107, 2006.
- SPARC CCMVal 2010: SPARC Report on the Evaluation of Chemistry-Climate Models, edited by Eyring, V.,

- 1310 Shepherd, T. G., and Waugh, D. W., SPARC, Toronto, Ontario, Canada, Tech. Rep. WCRP-132/WMO/TD-1526/SPARC Rep. 5, <http://www.atmos.physics.utoronto.ca/SPARC>, 2010.
- Starkov, G. V.: Statistical dependences between the magnetic activity indices, *Geomagn. Aeronomy*, 34, 101–103, 1994.
- Stiller, G. P., Tsidu, G. M., von Clarmann, T., Glatthor, N., Höpfner, M., Kellman, S., Linden, A., Ruhnke, R.,  
1315 Fischer, H., López-Puertas, M., Funke, B., and Gil-López, S.: An enhanced HNO<sub>3</sub> second maximum in the Antarctic midwinter upper stratosphere 2003, *J. Geophys. Res.*, 110, D20303, doi:10.1029/2005JD006011, 2005.
- Swider, W. and Keneshea, T. J.: Decrease of ozone and atomic oxygen in the lower mesosphere during a PCA event, *Planet. Space Sci.*, 21, 1969–1973, doi:10.1016/0032-0633(73)90126-8, 1973.
- 1320 Tiao, G. C., Reinsel, G. C., Xu, D., Pedrick, J. H., Zhu, X., Miller, A. J., DeLuisi, J. J., Mateer, C. L., and Wuebbles, D. J.: Effects of autocorrelation and temporal sampling schemes on estimates of trend and spatial correlation, *J. Geophys. Res.*, 95, 20,507–20,517, doi:10.1029/JD095iD12p20507, 1990.
- Tsyganenko, N. A., Usmanov, A. V., Papitashvili, V. O., Papitashvili, N. E., and Popov, V.: Software for computations of geomagnetic field and related coordinate systems, Special report, Soviet Geophysical Committee,  
1325 Moscow, USSR, 58 pp., 1987.
- Tunbridge, V. M., and Mitchell, N. J.: The two-day wave in the Antarctic and Arctic mesosphere and lower thermosphere, *Atmos. Chem. Phys.*, 9, 6377–6388, doi:10.5194/acp-9-6377-2009, 2009.
- Urban, J., Pommier, M., Murtagh, D. P., Santee, M. L., and Orsolini, Y. J.: Nitric acid in the stratosphere based on Odin observations from 2001 to 2009 – Part 1: A global climatology, *Atmos. Chem. Phys.*, 9, 7031–7044,  
1330 doi:10.5194/acp-9-7031-2009, 2009.
- Usoskin, I. G. and Kovaltsov, G. A.: Cosmic ray induced ionization in the atmosphere: Full modeling and practical applications, *J. Geophys. Res.*, 111, D21206, doi:10.1029/2006JD007150, 2006.
- Usoskin, I. G., Alanko-Huotari, K., Kovaltsov, G. A., and Mursula, K.: Hemispheric modulation of cosmic rays: monthly reconstruction for 1951–2004, *J. Geophys. Res.*, 110, A12108, doi:10.1029/2005JA011250,  
1335 2005.
- Usoskin, I. G., Kovaltsov, G. A., and Mironova, I. A.: Cosmic ray induced ionization model CRAC:CRII: An extension to the upper atmosphere, *J. Geophys. Res.*, 115, D10302, doi:10.1029/2009JD013142, 2010.
- Verronen, P. T., Seppälä, A., Kyrölä, E., Tamminen, J., Pickett, H. M., and Turunen, E.: Production of odd hydrogen in the mesosphere during the January 2005 solar proton event, *Geophys. Res. Lett.*, 33, L24811,  
1340 doi:10.1029/2006GL028115, 2006.
- Vogel, B., Konopka, P., Groöß, J.-U., Müller, Funke, B., López-Puertas, M., Reddmann, T., Stiller, G., von Clarmann, T., and Riese, M.: Model simulations of stratospheric ozone loss caused by enhanced mesospheric NO<sub>x</sub> during Arctic winter 2003/2004, *Atmos. Chem. Phys.*, 8, 5279–5293, doi:10.5194/acp-8-5279-2008, 2008.
- 1345 Warneck, P.: Cosmic radiation as a source of odd nitrogen in the stratosphere, *J. Geophys. Res.*, 77, 6589–6591, doi:10.1029/JC077i033p06589, 1972.
- WDC website: <http://wdc.kugi.kyoto-u.ac.jp>, 2008.
- White, W. B.: Response of tropical global ocean temperature to the Sun's quasi-decadal UV radiative forcing of the stratosphere, *J. Geophys. Res.*, 111, C09020, doi:10.1029/2004JC002552, 2006.

- 1350 White, W. B., Lean, J., Cayan, D. R., and Dettinger, M. D.: Response of global upper ocean temperature to changing solar irradiance, *J. Geophys. Res.*, 102, 3255–3266, doi:10.1029/96JC03549, 1997.
- World Meteorological Organization (WMO)/United Nations Environment Programme (UNEP): Scientific Assessment of Ozone Depletion: 2002, Global Research and Monitoring Project – Report No. 47, Geneva, Switzerland, 489 pp., 2003.
- 1355 Wolter, K. and Timlin, M. S.: Measuring the strength of ENSO events: How does 1997/98 rank?, *Weather*, 53, 315–324, 1998.
- Yoden, S., Taguchi, M., and Naito, Y.: Numerical studies on time variations of the troposphere-stratosphere coupled system, *J. Met. Soc. Japan*, 80, 811–830, 2002.

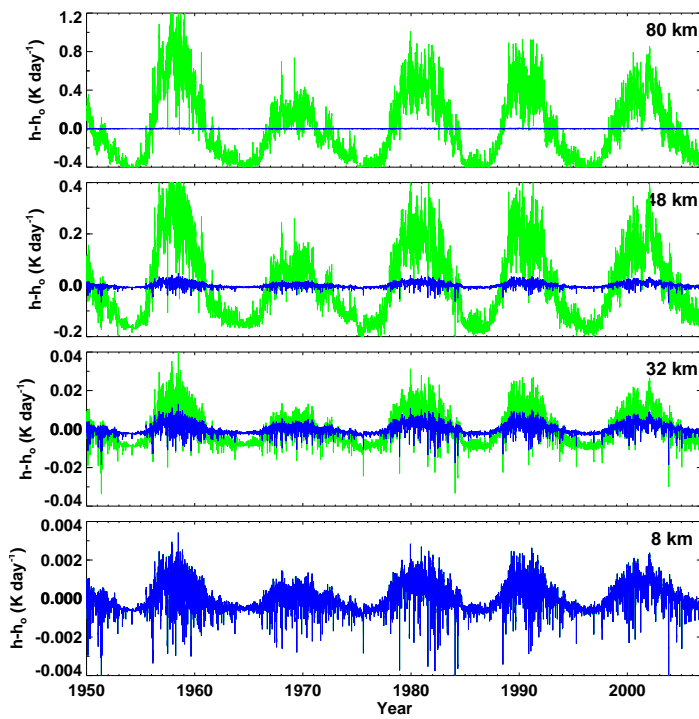


**Fig. 1.** Time series of the solar heating rate deviation from the 1950–2006 mean values in the troposphere (8 km), stratosphere (32 km), near the stratopause (48 km) and in the mesosphere (80 km). Blue: variability only in TSI is taken into account; green: variability in SSI is taken into account. An overhead Sun and equatorial ozone profile are considered in calculating the solar heating rates.

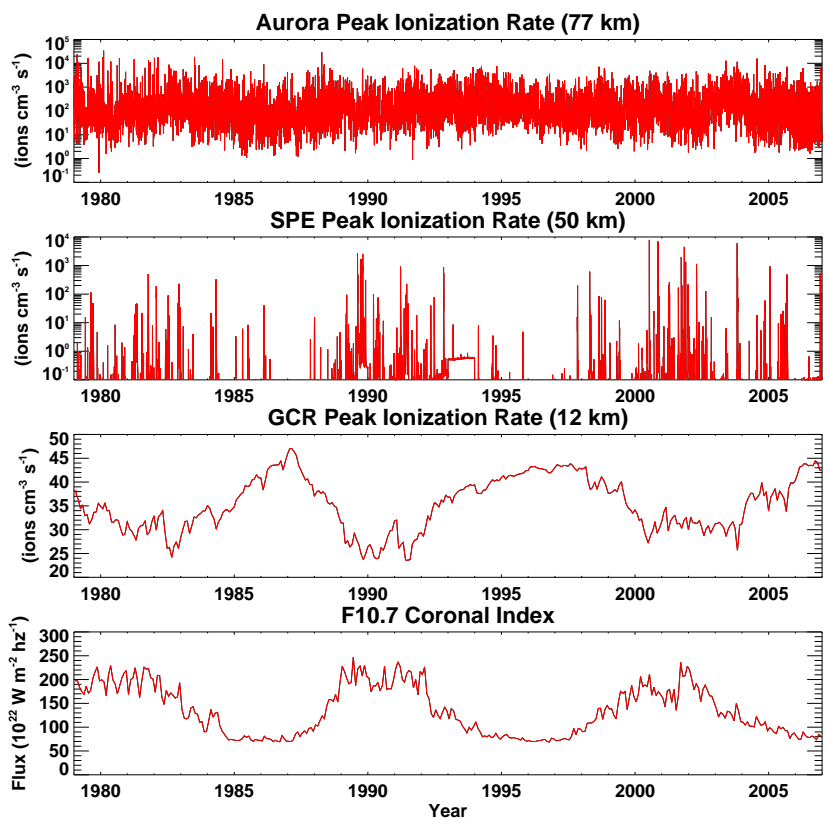
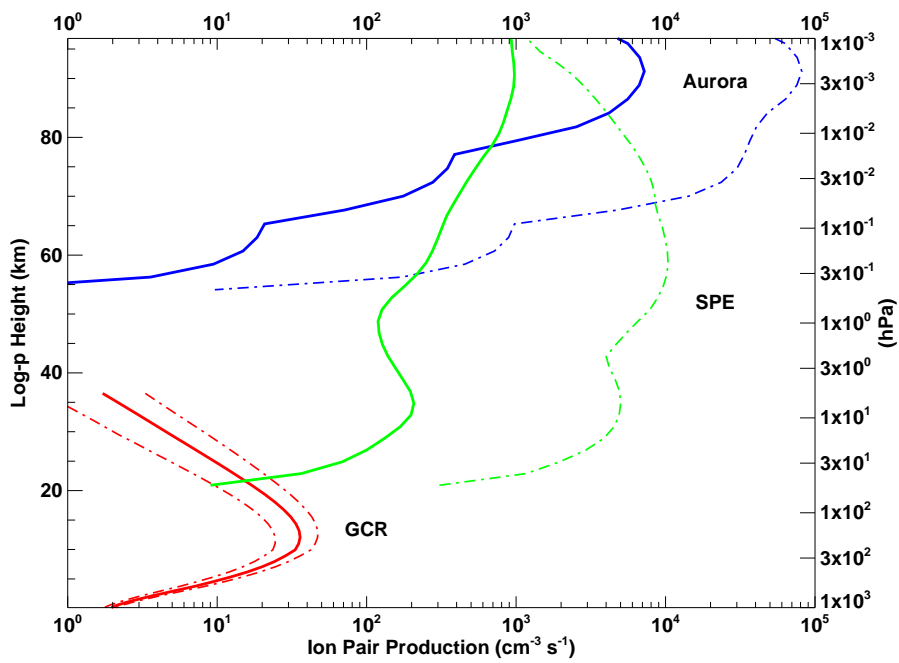
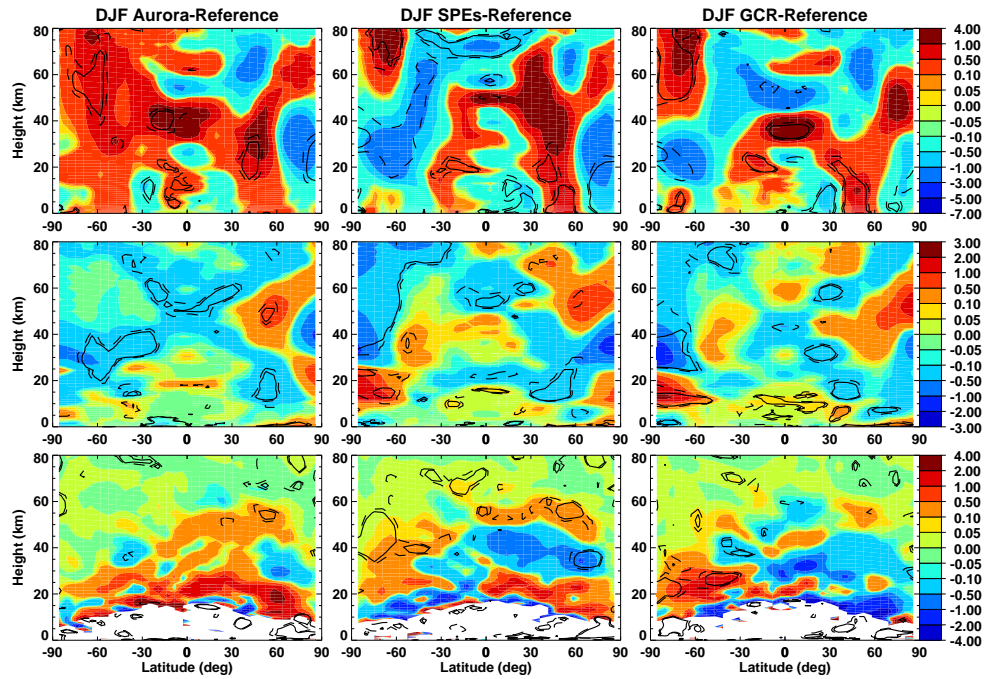


Fig. 2. Timeseries of peak daily ion pair production for aurora, SPEs and GCR. F10.7 variation is shown in the bottom panel.



**Fig. 3.** Vertical pressure profiles of the time mean ion pair production rate for aurora (blue), SPEs (green), and GCR (red). The time average for SPEs is done only for the fraction of the time when ionization exceeds  $100 \text{ pairs cm}^{-3} \text{s}^{-1}$ . The dash-dot curves represent maximum and minimum ionization for the 1979 through 2006 period. Minimum ionization is significant only for GCR.



**Fig. 4.** Run mean, December–February mean differences compared to the reference run for aurora (left), SPEs (center) and GCR (right) showing zonal wind (top, m/s), temperature (middle, K) and mass streamfunction (bottom, kg/m/s, values outside the range  $(-4.4)$  not plotted). Solid and dashed contours denote regions with 95% and 90% confidence levels, respectively. These two contours are the same for all subsequent figures.

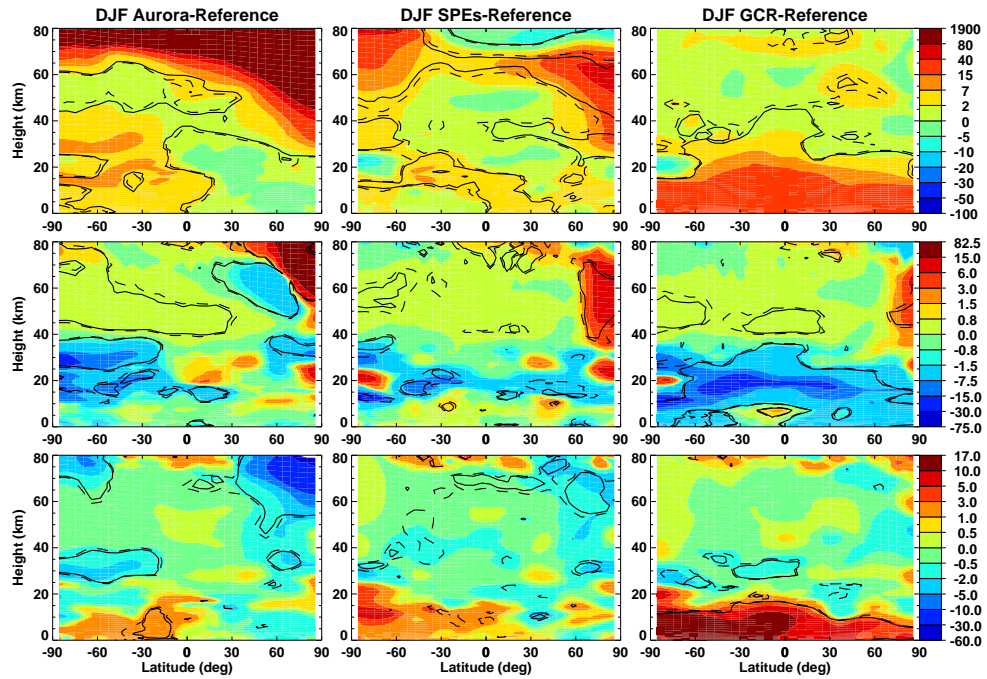


**Fig. 5.** Run mean, December–February mean NO<sub>y</sub> (top), HO<sub>x</sub> (middle) and O<sub>3</sub> (bottom) differences for aurora, SPEs and GCR runs compared to the reference run (%).

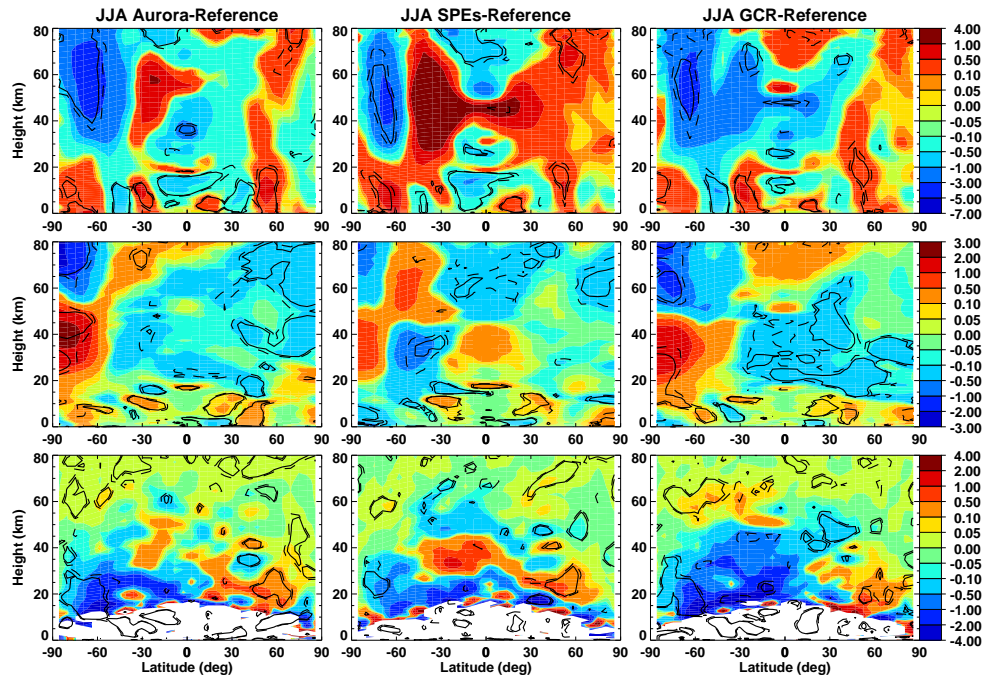


**Fig. 6.** Run mean, June–August mean differences compared to the reference run for aurora (left), SPEs (center) and GCR (right) showing zonal wind (top, m/s), temperature (middle, K) and mass streamfunction (bottom, kg/m/s, values outside the range  $(-4.4)$  not plotted). 47

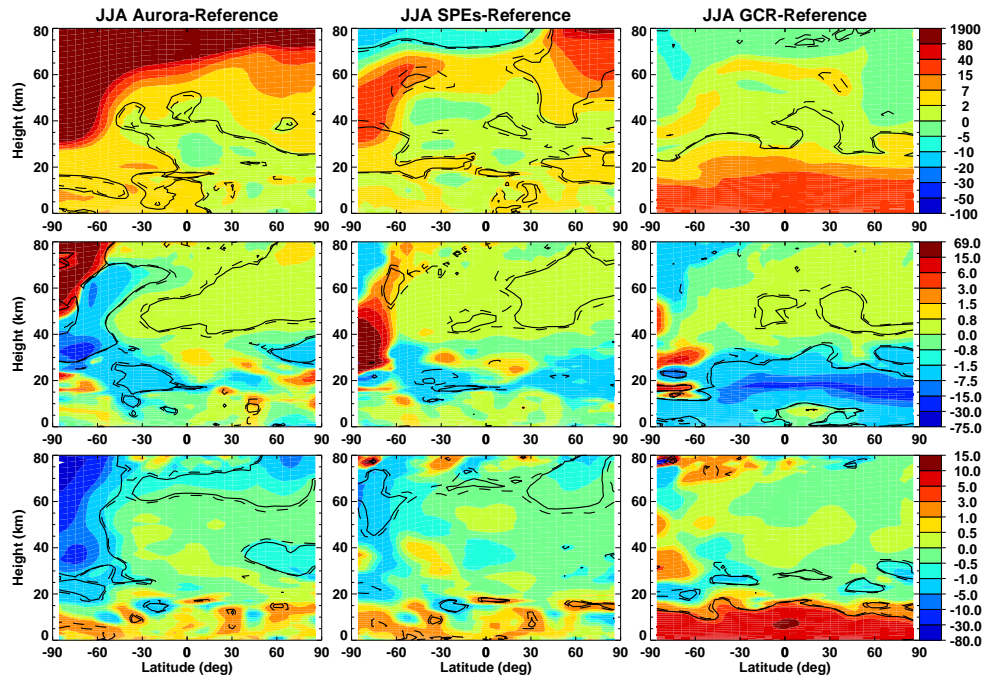


**Fig. 7.** Run mean, June–August mean compared to the reference run for aurora (left), SPEs (center) and GCR (right) showing  $\text{NO}_y$  (top),  $\text{HO}_x$  (middle) and  $\text{O}_3$  (bottom) (%).

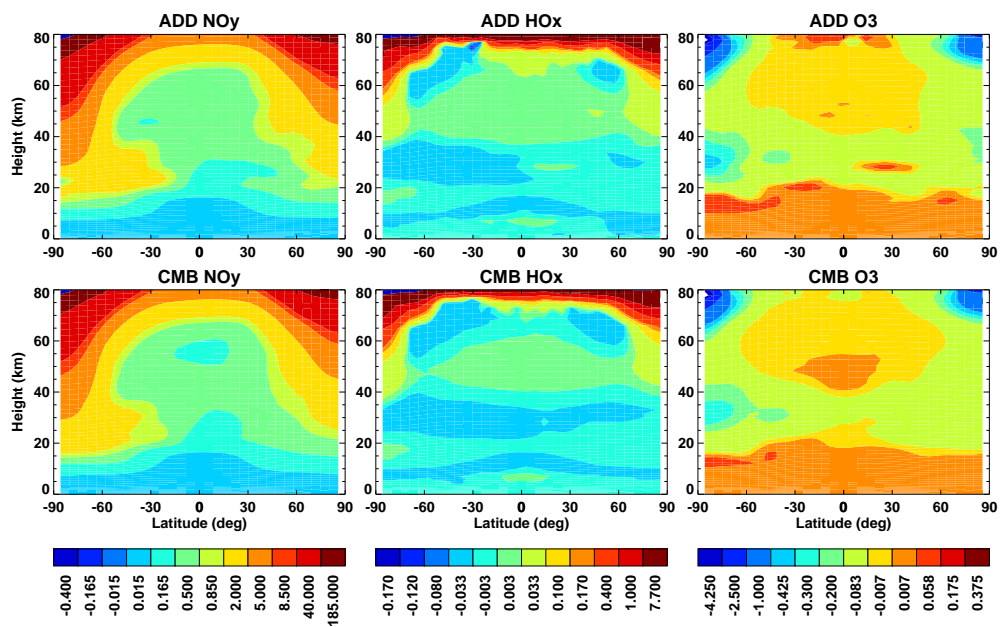


**Fig. 8.** Run mean, annual mean difference from the reference run for NO<sub>y</sub> (left, ppbv), HO<sub>x</sub> (middle, ppbv) and O<sub>3</sub> (right, ppmv). Top panels: sum for the individual aurora, SPEs and GCR runs. Bottom panels: combined run.

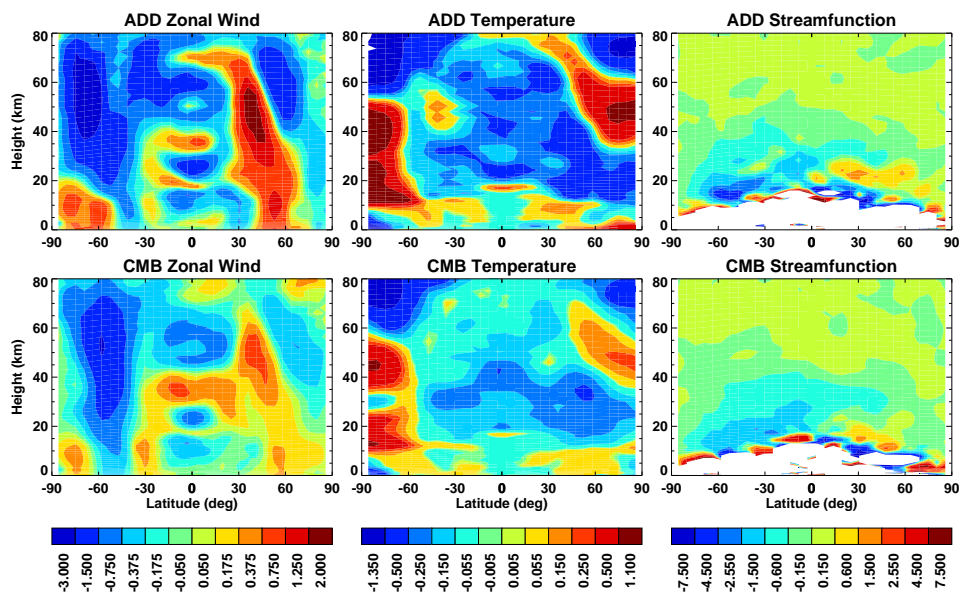


**Fig. 9.** Run mean, annual mean difference from the reference run for zonal wind (left), temperature (middle) and mass streamfunction (right, values outside the  $(-9.9)$  interval not plotted). Top panels: sum for the aurora, SPEs and GCR runs. Bottom panels: combined run.

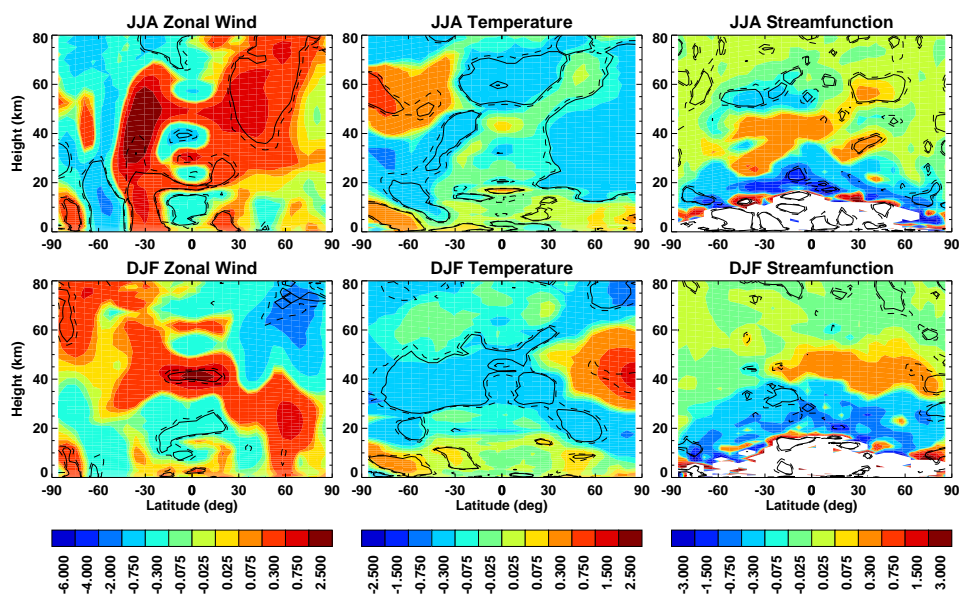


**Fig. 10.** June–August run mean, ensemble mean (top) and December–February run mean, ensemble mean (bottom) zonal wind (m/s), temperature (K), and mass streamfunction (kg/m/s, values outside the range  $(-4.4)$  not plotted) differences for the combined EPP ensemble run compared to the reference ensemble run.

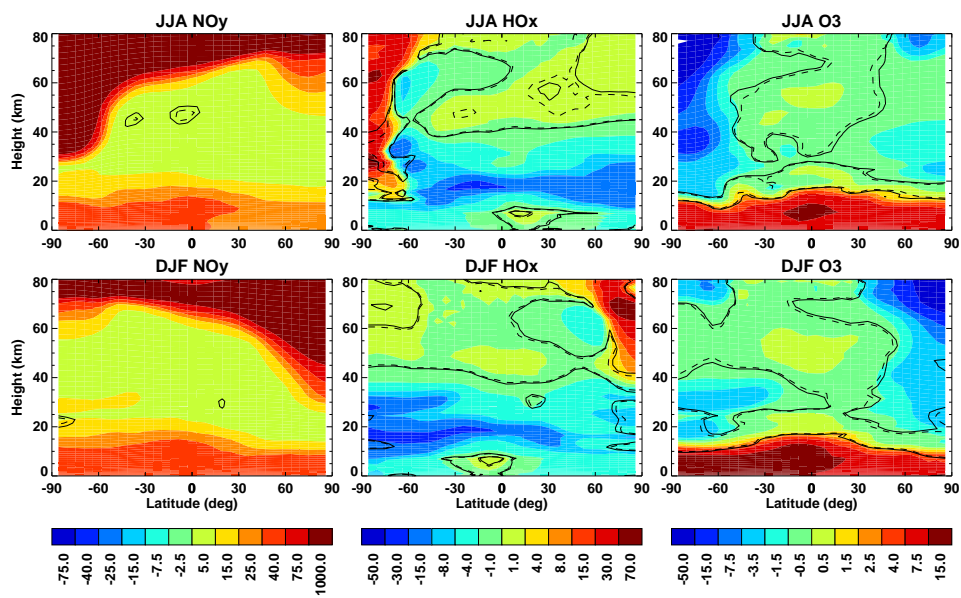


**Fig. 11.** June–August run mean, ensemble mean (top) and December–February run mean, ensemble mean (bottom) NO<sub>y</sub>, HO<sub>x</sub> and O<sub>3</sub> differences for the combined EPP ensemble run compared to reference ensemble run (%).

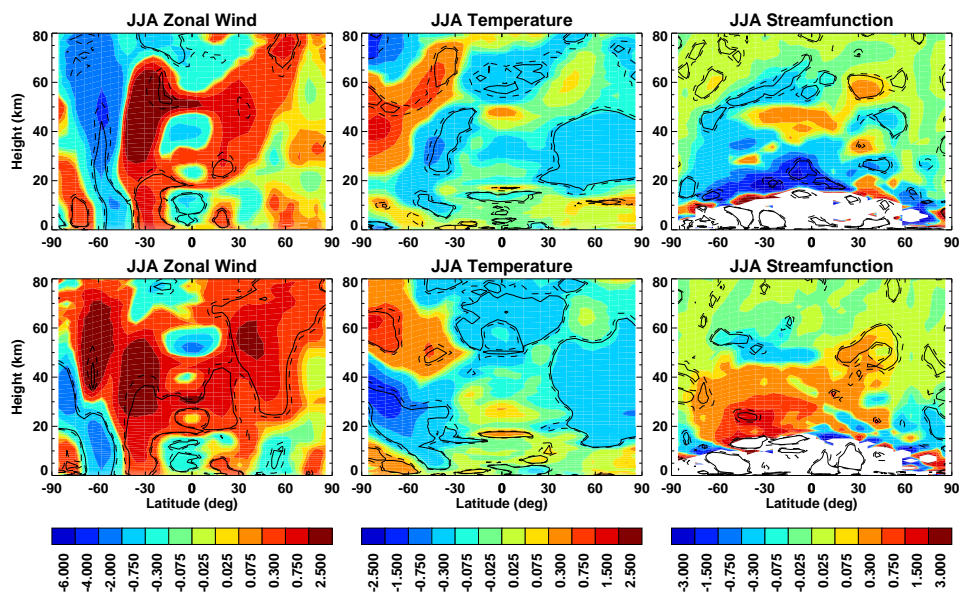


**Fig. 12.** June–August run mean difference of zonal wind, temperature and mass streamfunction from the ensemble reference run for two of the combined EPP ensemble members. Top, weak vortex case. Bottom, strong vortex case.

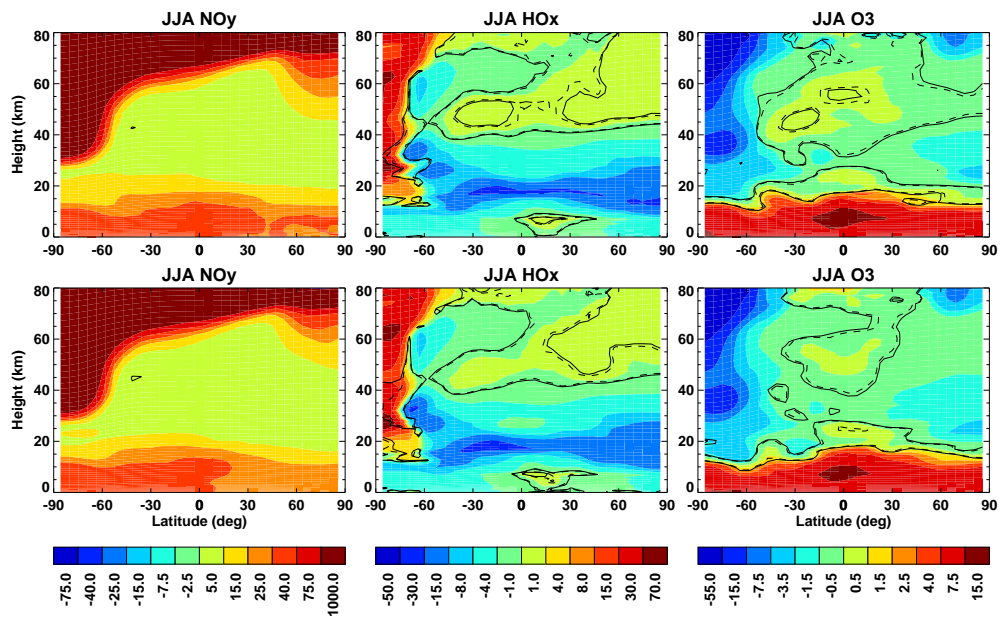


**Fig. 13.** As in Fig. 12 but for NO<sub>y</sub>, HO<sub>x</sub> and O<sub>3</sub> differences (%).

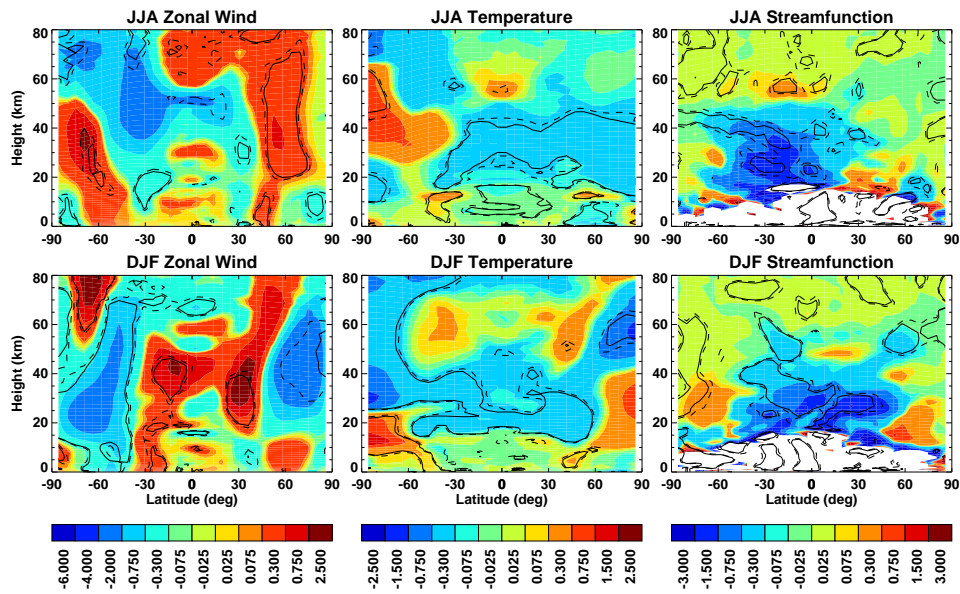


**Fig. 14.** June–August run mean, ensemble mean (top) and December–February run mean, ensemble mean (bottom) zonal wind (m/s), temperature (K), and mass streamfunction (kg/m/s, values outside the range  $(-4.4)$  not plotted) differences for the solar variability combined with EPP ensemble run compared to the solar variability only ensemble run.

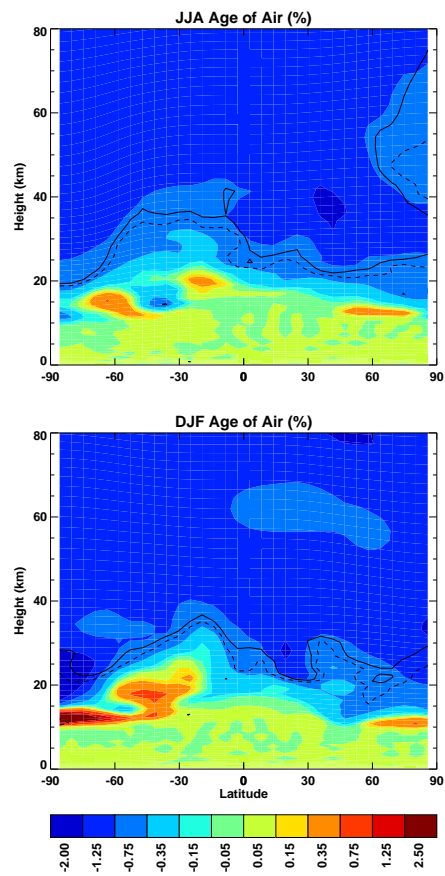
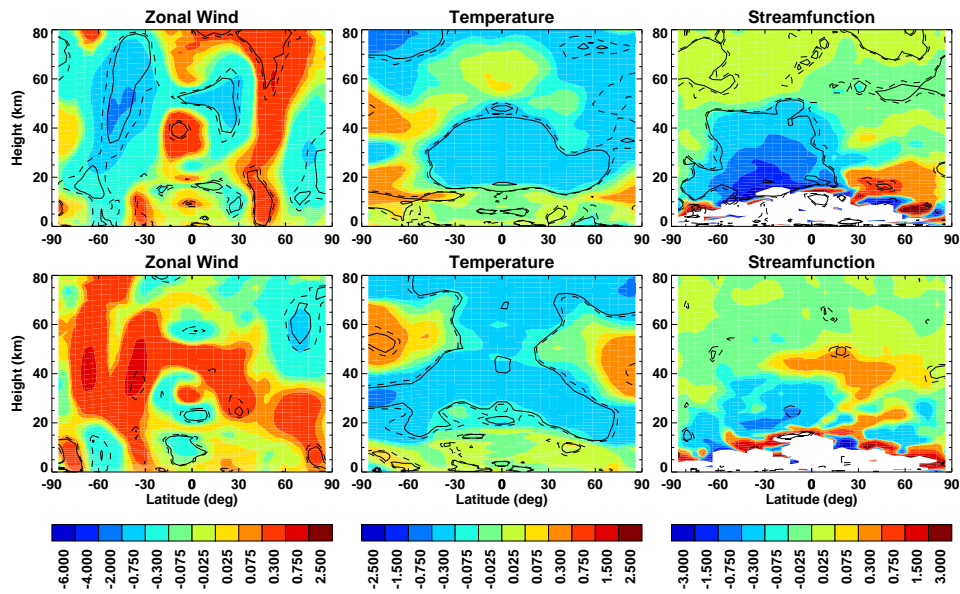
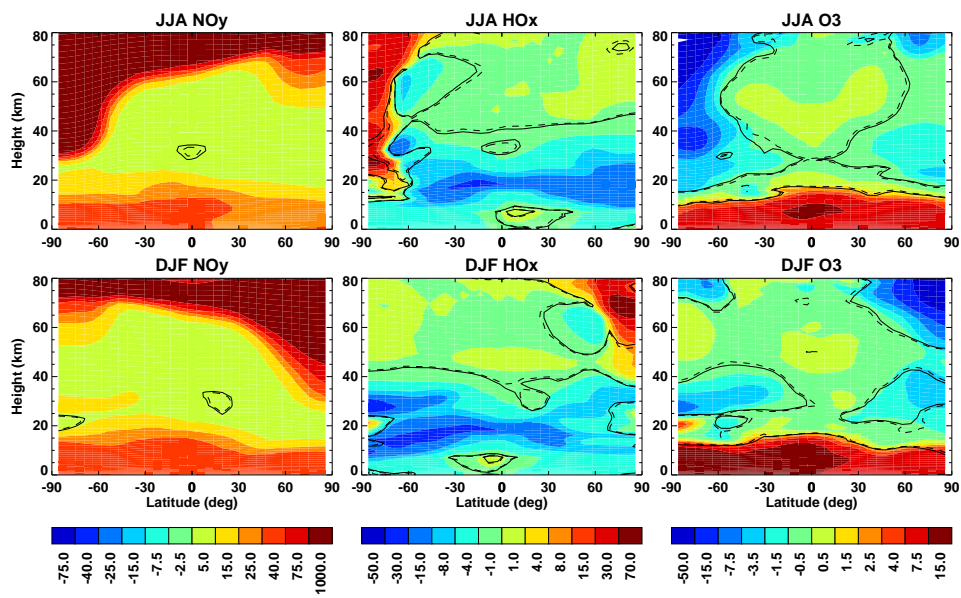


Fig. 15. Run mean, ensemble mean age of air (%) difference between the two ensembles shown in Fig. 14.



**Fig. 16.** Comparison of run mean, ensemble mean, annual mean difference from the reference ensembles of zonal wind (m/s) (left), temperature (K) (middle) and mass streamfunction (kg/m/s) (right). Top panels are for solar variability with EPP vs. solar variability only ensemble. Bottom panels are for the EPP without solar variability vs. the no EPP and no solar variability reference ensemble.



**Fig. 17.** Run mean, ensemble mean NO<sub>y</sub>, HO<sub>x</sub> and O<sub>3</sub> differences (%) between the two ensembles shown in Fig. 14.

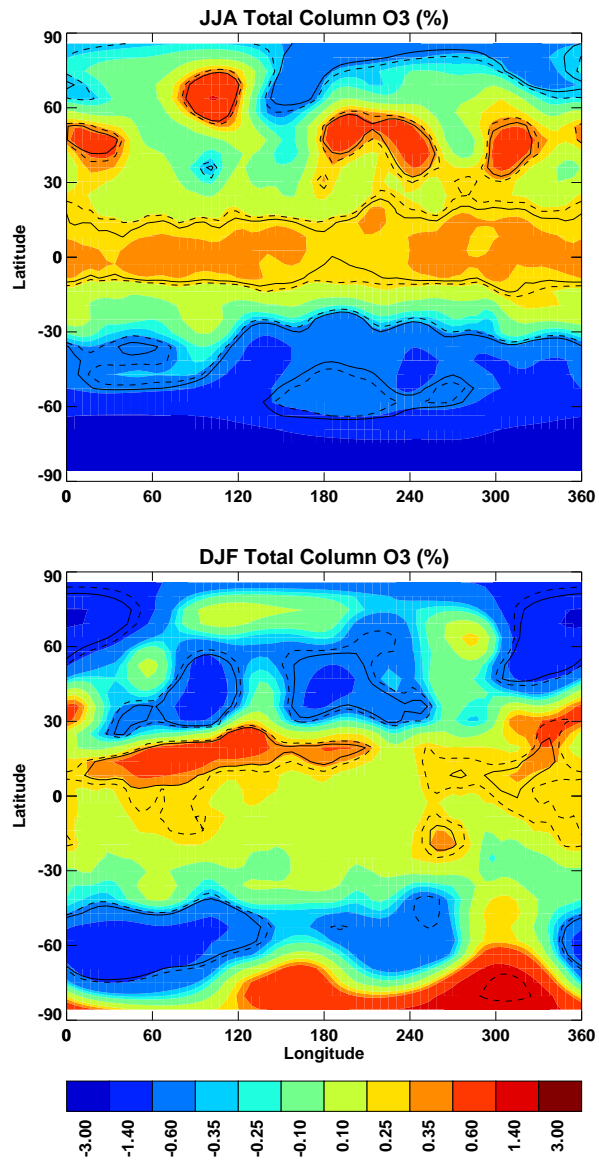


**Fig. 18.** Run mean, ensemble mean total column ozone (%) difference between the two ensembles shown in Fig. 14.

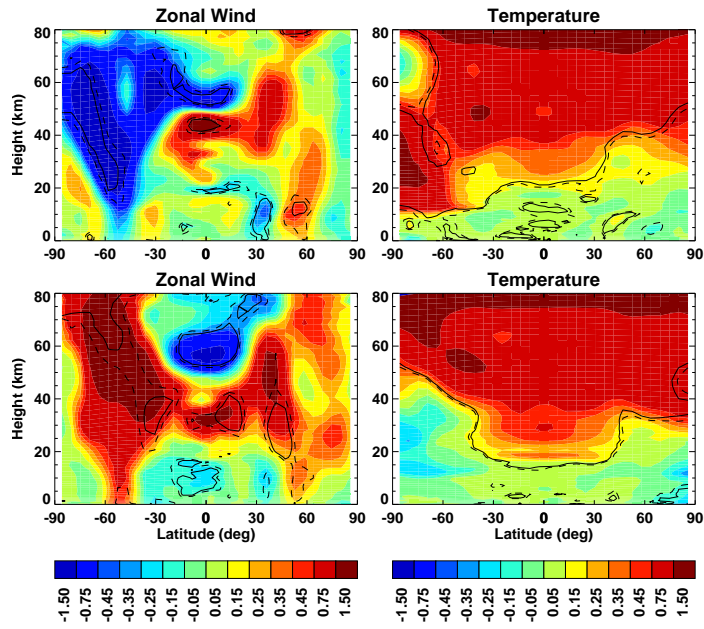


**Fig. 19.** Latitude-altitude **dependence of the annual mean** regression coefficient for the solar variability only ensemble mean (top) and for the combined solar variability and EPP ensemble mean (bottom): (per 100 units of F10.7) left, zonal mean wind (m/s) and right, zonal mean temperature (K).

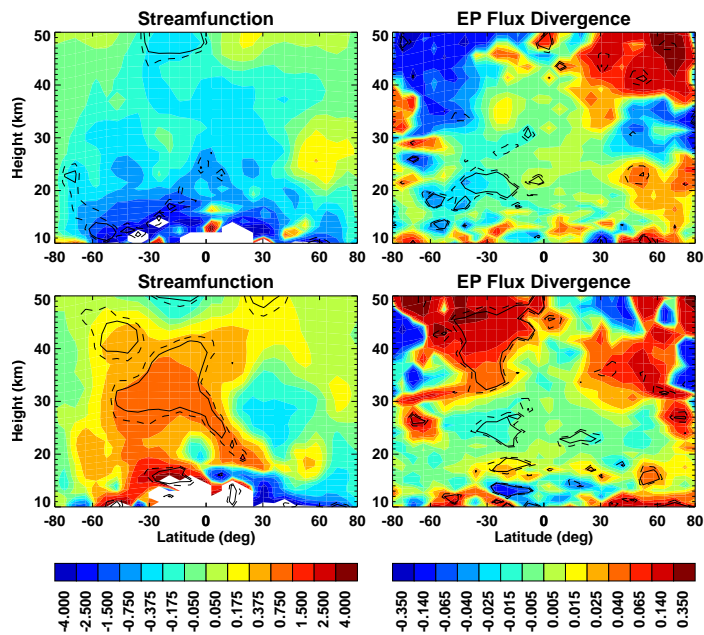


**Fig. 20.** Latitude-altitude **dependence of the annual mean** regression coefficient for the solar variability only ensemble mean (top) and for the combined solar variability and EPP ensemble mean (bottom): (per 100 units of F10.7) left, mass streamfunction (kg/m/s, values outside the range (-5,5) are not plotted) and right, Eliassen-Palm flux divergence (m/s/s).

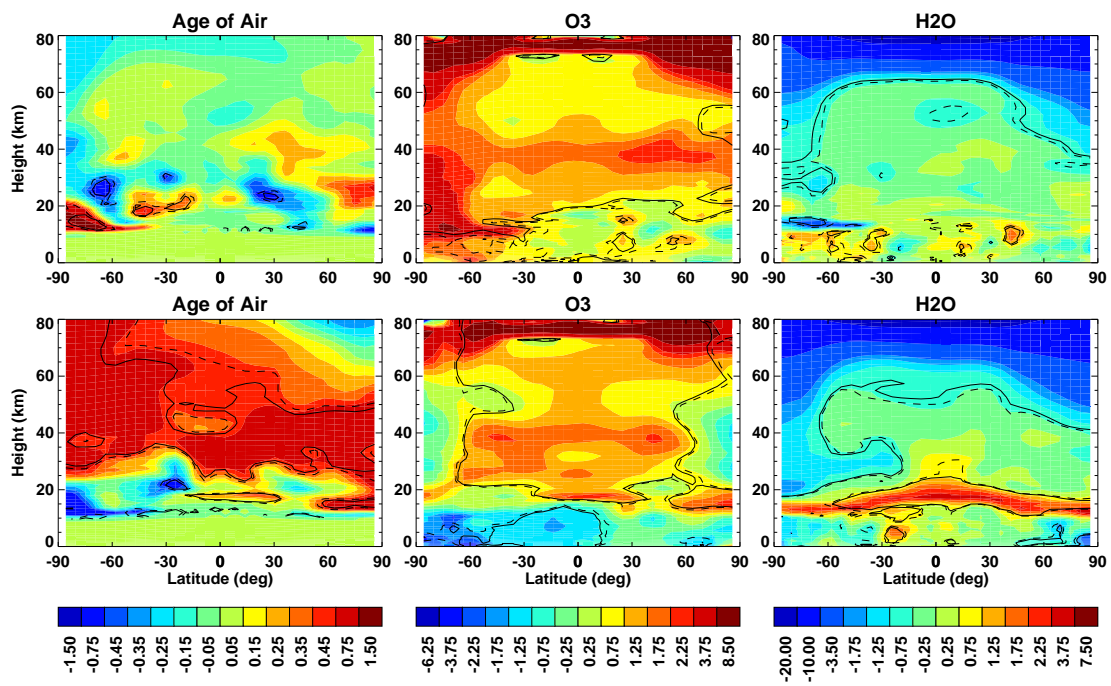
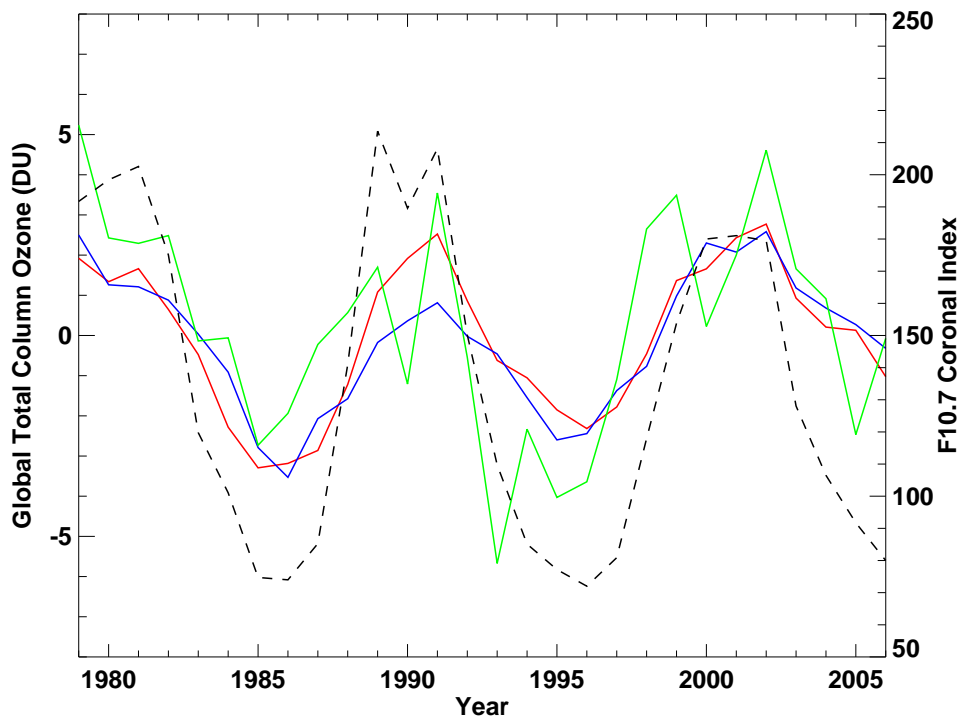
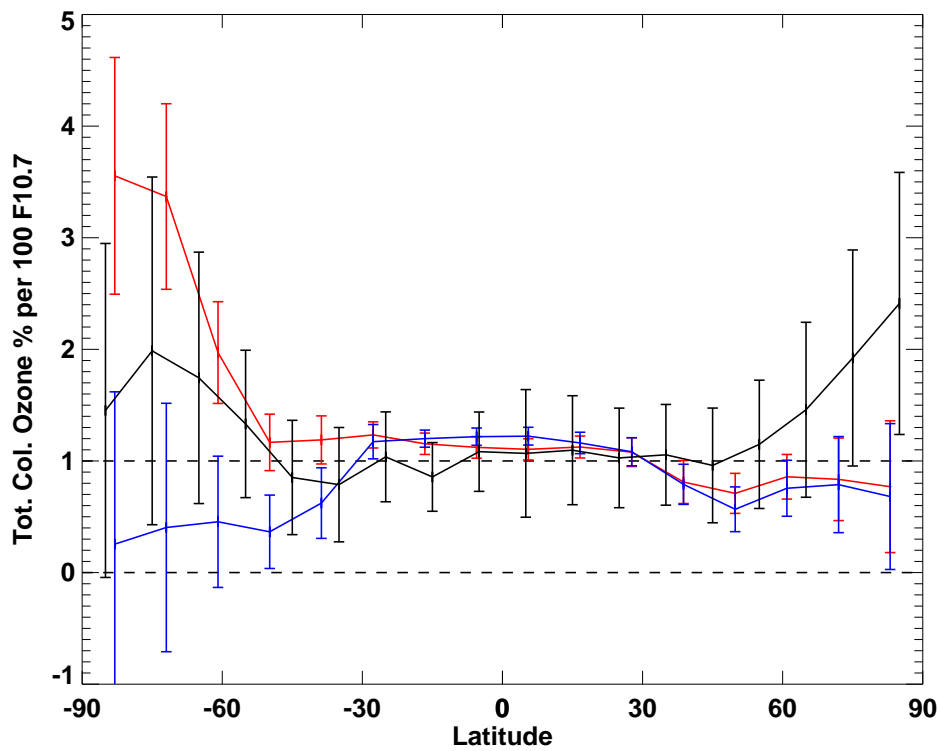


Fig. 21. As in Fig. 19 but for age of air (left), O<sub>3</sub> (middle), and H<sub>2</sub>O (right). Differences in %.



**Fig. 22.** Annual mean, global mean timeseries of the total column  $O_3$  regression fit consisting of the F10.7 index term and the residual term for the solar variability ensemble without EPP (red), the solar variability ensemble with EPP (blue) and observed total column ozone data from Fioletov et al. (2002) (green). The F10.7 index is also shown (dashed).



**Fig. 23.** Zonal mean total column  $O_3$  regression fit against the F10.7 index for the ensemble without EPP (red) and the ensemble with EPP (blue). Regression of observed total column ozone from Fioletov et al. (2002) is also shown (black). The column  $O_3$  response is in % per 100 units of F10.7. Error bars are  $\pm 2\sigma$ . The two dashed lines show the 0% and 1% levels.

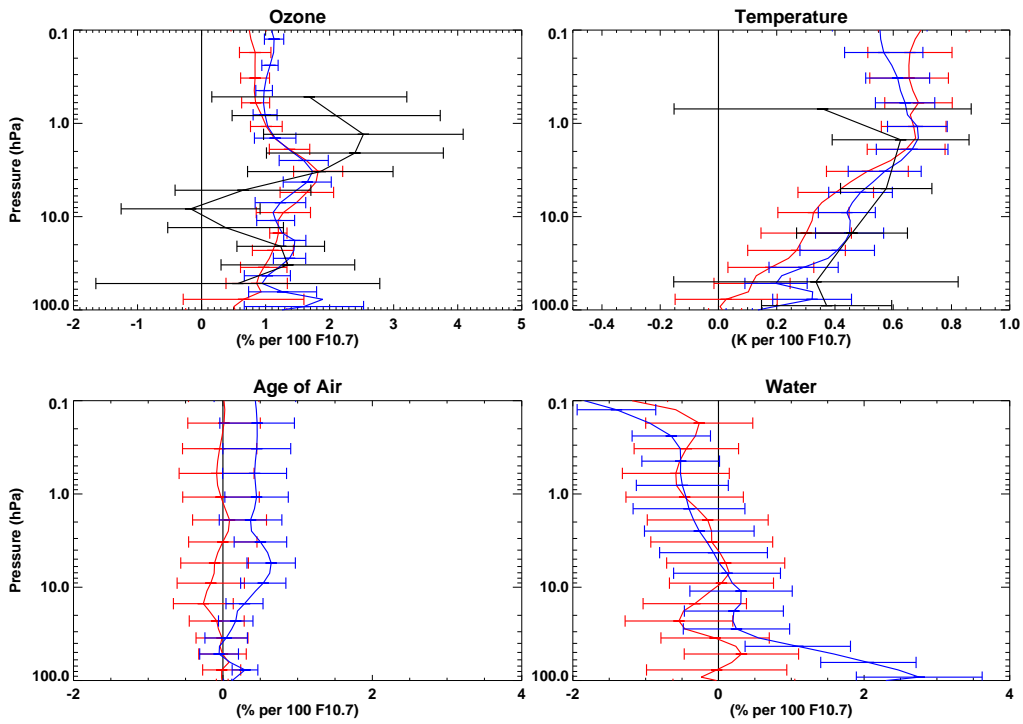


**Fig. 24.** Tropical mean, 25° S–25° N, ozone, temperature, age of air and water vapour regression fits to the F10.7 index for the ensemble without EPP (red) and the ensemble with EPP (blue). Regression fits for observed ozone (SAGE corrected SBUV, McLinden et al., 2009) and SSU/MSU temperature (Randel et al., 2009) are also shown (black). Horizontal axis values are % per 100 units of F10.7 except for temperature which is in K. Error bars are  $\pm 2\sigma$ .